Kyoto University

Master Thesis

Research and Development of Large-Aperture Hybrid Photo-Detector for Hyper-Kamiokande

Author:
Miao Jiang

Supervisor:
Prof. Tsuyoshi Nakaya

A thesis submitted in fulfilment of the requirements
for the degree of Master of Science

in the

High Energy Physics Group
Department of Physics

October 2015

KYOTO UNIVERSITY

Abstract

Faculty of Science
Department of Physics

Master of Science

Research and Development of Large-Aperture Hybrid Photo-Detector for Hyper-Kamiokande

by Miao JIANG

Hyper-Kamiokande (Hyper-K) is a proposed next generation underground water Cherenkov detector. As one of photo-detector candidates, a hybrid photo-detector (HPD), which is composed of a phototube and an avalanche diode (AD), is under development. The manufacture cost of HPD is expected to be low because of the simple structure of AD. Moreover, the fast drift time of electron and the large bombardment gain of HPD bring a good timing resolution and high photoelectron detection efficiency.

We developed the 20cm HPD with ϕ5 mm AD [1], 50 cm HPD with ϕ5 mm AD [2], 50 cm HPD with ϕ20 mm AD in order and evaluated their performance.

We confirmed that the gain temperature dependency ($\sim$ 2%/°C) of the 20 cm HPD with ϕ5 mm AD and the 50 cm HPD with ϕ5 mm AD will not influence its stability in Hyper-K.

We also confirmed that 50 cm HPD with ϕ5 mm AD has a transit time spread of is 1.15 ns, which is better than that of Super-K PMT (2.2ns), and a dark count rate of 0.8 kHz at room temperature, which gives an estimated value of 4.65 kHz on the dark count rate of the 50 cm HPD with ϕ20 mm AD at Hyper-K temperature ($\sim$ 13 °C). The output linearity is kept until 140 photoelectron within maximum deviation of 6%.

The 50 cm HPD with ϕ20 mm AD, our target design, has a low S/N due to the large AD junction capacitance. Two proposed solutions, the segmented AD and the transformer decoupling have been tested and showed good result: the 1p.e resolution reaches to 28% and 51.7% respectively. The development of 50 cm HPD with ϕ20 mm AD is still ongoing.

To conclude, the 50 cm HPD with ϕ20 mm AD has great potential as a Hyper-Kamiokande photo-detector. It will be ready in 2016.

Acknowledgements

I would like to express my great appreciation to my supervisor Prof. Tsuyoshi Nakaya for his overall support. Through discussion with him, I could understand my work more deeply. Without his advices, this thesis would not exist.

My heartfelt appreciation goes to Dr. Akihiro Minamino, who is also my supervisor and shared an office with me in Kyoto, and Dr. Yasuhiro Nishimura, who is the convener of the Photosensor development group in Hyper-K and Prof. Atsuko Ichikawa, who gave me lots of helpful comments on this thesis. Their insightful advice and warm encouragements helped me a lot.

I am cordially thankful to Ms. Seiko Hirota, Mr. Yusuke Suda, Mr. Yuji Okajima, who helped me on the evaluation and analysis of the HPD. Ms. Seiko Hirota and Mr. Yusuke Suda taught me how to operate HPD, how to take and analyze data and how to publish result to others. Mr. Yuji Okajima taught me how to use the modules and computer in Kamioka Observatory.

I must thank to Prof. Masato Shiozawa, Prof. Yoshinari Hayato, Dr. Shoei Nakayama, Dr. Hidekazu Tanaka, Prof. Masahiro Kuze and Dr. Akimichi Taketa for their guidance and supervision.

I am indebted to the members of Hamamatsu Photonics K.K. Dr. Yoshihiko Kawai, Mr. Takayuki Ohmura and Mr. Masatoshi Suzuki, especially for the development of HPD and high-QE PMT.

My appreciation also goes to the members of High Energy Physics Laboratory, Prof. Masaya Ishino, Dr. Hajime Nanjo, Dr. Kiseki Nakamura, Dr. Tatsuya Kikawa, Dr. Takahiko Masuda, Mr. Yosuke Maeda, Mr. Kunxian Huang, Mr. Kento Suzuki, Mr. Daichi Naito, Mr. Takahiro Hiraki, Mr. Shota Takahashi, Mr. Shigeto Seki, Mr. Takuya Tashiro, Mr. Naoyuki Kamo, Mr. Ichinori Kamiji, Mr. Takuto Kunigo, Mr. Kota Nakagiri, Mr. Keigo Nakamura, Mr. Tasuya Hayashino, Mr. Kento Yoshida and Mr. Yuki Ishiyama for my fulfill and happy life in Kyoto. I would like to thank Ms. Eriko Hayashi who supports our laboratory for her fantastic assist.

Also, I appreciate the financial support from Ministry of Education, Culture, Sports, Science and Technology of Japan (MEXT).

Finally, I would like thank to my family and all my friends.

Contents

Abstract i

Acknowledgements ii

Contents iii

List of Figures vi

List of Tables viii

Abbreviations ix

1 Introduction 1
- 1.1 Neutrino Oscillation . . . 1
- 1.2 Mass hierarchy & Leptonic CP violation . . . 3
- 1.3 Neutrino detection . . . 5
  - 1.3.1 Principle of Water-Cherenkov detector . . . 6
  - 1.3.2 Water-Cherenkov detector in neutrino physics experiment . . . 7
- 1.4 Hyper-Kamiokande project . . . 8
- 1.5 Other physics topics of Hyper-Kamioaknde . . . 10
  - 1.5.1 Nucleon decay . . . 10
  - 1.5.2 Astrophysics using neutrinos . . . 10

2 Development of new photo-detector for Hyper-K 12
- 2.1 Requirements for the photosensor in Hyper-K . . . 12
  - 2.1.1 Single photon detection efficiency . . . 13
  - 2.1.2 Single photon energy resolution . . . 14
  - 2.1.3 Single photon timing resolution . . . 16
  - 2.1.4 Dark count rate . . . 17
  - 2.1.5 Linearity and wide dynamic range . . . 18
  - 2.1.6 Other important characteristics . . . 19
- 2.2 Candidates of new Photosensor . . . 19
- 2.3 High-QE photocathode development . . . 20
- 2.4 Schedule of development . . . 21
- 2.5 Hybrid Photo-Detector . . . 21
  - 2.5.1 Principle of avalanche diode . . . 22
- 2.6 HPD system used in this thesis . . . 23

2.7 Goal of this thesis . . . 25

3 Performance evaluation of HPD with ϕ5 mm AD 28
3.1 The Temperature dependency of 20cm HPD with ϕ5 mm AD . . . 28
3.1.1 Method . . . 29
3.1.2 The temperature dependence of gain . . . 29
3.1.3 The temperature dependence of single photoelectron charge resolution . . . 31
3.1.4 The temperature dependence of peak/valley of the HPD . . . 32
3.1.5 The temperature dependence of dark count rate of the HPD . . . 33
3.2 Performance Evaluation of 50 cm HPD with ϕ5mm AD . . . 33
3.2.1 Signal response of single p.e. . . . 34
3.2.2 Transit time spread . . . 35
3.2.3 Linearity . . . 37
3.2.3.1 Linearity measurement in low luminosity . . . 37
3.2.3.2 Linearity measurement in high luminosity and dynamic range . . . 37
3.2.4 Dark count rate . . . 39
3.2.5 Temperature dependency of gain . . . 40
3.3 Summary of the performance evaluation of HPD with ϕ5 mm AD . . . 41

4 R&D of 50 cm HPD with a large area AD 43
4.1 Application of segmented AD . . . 45
4.1.1 Segmented AD . . . 45
4.1.2 Evaluation on 50 cm HPD . . . 45
4.2 Application of decoupling transformer . . . 47
4.2.1 Principle . . . 47
4.2.2 Evaluation on a single AD . . . 49
4.2.3 Evaluation on 50 cm HPD with a ϕ14.7 mm AD . . . 51
4.2.3.1 Response of multiple photoelectrons . . . 51
4.2.3.2 Transit time spread . . . 53
4.2.3.3 Dark count rate . . . 56
4.2.3.4 Effect of a co-axis signal cable . . . 57
4.3 Summary of R&D of 50 cm HPD with a large area AD . . . 59

5 R&D of High Voltage Supply 60
5.1 Selection of high voltage module . . . 60
5.1.1 Performance evaluation after installed into HPD . . . 60
5.2 External HV supply . . . 61
5.3 On-off resistant . . . 61
5.4 Summary of R&D of High Voltage supply . . . 63

6 Summary and future prospects 64
6.1 Summary . . . 64
6.2 Future prospects . . . 66

Bibliography **67**

List of Figures

1.1 Image of a charged particle emitting Cherenkov light . . . 6
1.2 T2K experiment . . . 7
1.3 Super Kamiokande detector . . . 8
1.4 Internal view of the tank of the Super Kamiokande detector . . . 9
1.5 Hyper-Kamiokande detecotr . . . 9
1.6 Cross section of Hyper-Kamiokande detector . . . 10

2.1 Photon electron response pulse height distribution of a 50 cm HPD prototype . . . 14
2.2 First stage gain as a function of the accelerating voltage [3] . . . 15
2.3 The time difference due to different light path . . . 17
2.4 Three candidates of the photo-sensors for Hyper-K (provided by Hamamatsu) . . . 20
2.5 Comparison on QE between High QE version PMT and Normal QE version PMT (provided by Hamamatsu) . . . 20
2.6 Development schedule of photon sensor for Hyper-Kamiokande . . . 21
2.7 Principle of an HPD amplification and typical values of the 20cm HPD. . . . 22
2.8 20cm HPD . . . 24
2.9 20cm HPD without any accessories . . . 24
2.10 5mm AD . . . 24
2.11 The schematic view of the circuit in the HPD . . . 25
2.12 The control power supply . . . 26

3.1 Setup to measure temperature dependency . . . 29
3.2 The signal distribution of an 20cm HPD . . . 30
3.3 An example of the temperature dependence measurement of the HPD . . . 30
3.4 The temperature dependence of the gain of the HPD with preamplifier (left) and that of the AD (right) . . . 31
3.5 The temperature dependence of the single p.e. charge resolution of HPD (left) and the contribution from AD's noise (right) . . . 32
3.6 The temperature dependence of peak/valley of the HPD . . . 34
3.7 The temperature dependence of dark count rate of the HPD . . . 34
3.8 Setup for the transit time spread measurement . . . 35
3.9 The relationship between the charge output of HPD and the time of signal appearance . . . 36
3.10 The relationship between the luminosity and the TTS of HPD . . . 36
3.11 Gain Linearity in low luminosity . . . 37
3.12 Setup for the gain linearity measurement in high luminosity . . . 38

3.13 Principle of the gain linearity measurement in high luminosity 38
3.14 Relationship between output charge and luminosity 39
3.15 The change of the deviation from the linear assumption with luminosity . 39
3.16 The relationship between dark count rate of HPD and threshold 40
3.17 Temperature dependency of gain of 50 cm HPD with 5mm AD 41

4.1 The HPD system with multi-ch AD 45
4.2 Multi-channel AD 46
4.3 Pulse shape of 50 cm HPD with 5ch 20mm AD (red) and 50 cm HPD with 5mm AD (blue) 46
4.4 Integral Charge distribution of 50 cm HPD with 5ch 20mm AD 47
4.5 Principle of the capacitance suppression using decoupling transformer . . 48
4.6 Ideal transformer coupling between AD and preamplifier[4] 48
4.7 Circuit for the test of the preamplifier with the decoupling transformer on a single ϕ20 mm AD 49
4.8 Pulse shape of a single ϕ20 mm AD output 50
4.9 The pulse height distribution of the pedestal 50
4.10 The pulse height distribution of the signal in high luminosity 51
4.11 The integral charge distribution of the pedestal 52
4.12 The integral charge distribution of the signal in high luminosity 53
4.13 Circuit of the 50 cm HPD using decoupling transformer 53
4.14 The effect of decoupling transformer on pulse shape of HPD signal 54
4.15 The effect of decoupling transformer on the integral charge distribution of HPD signal 54
4.16 The effect of decoupling transformer on the pulse height distribution of HPD signal 55
4.17 Integral charge distribution of the signal of the 50 cm HPD with ϕ14.7 mm AD with decoupling transformer 55
4.18 Transit time distribution of 50 cm HPD with 14.7 mm AD and the decoupling transformer 56
4.19 Transit time spread σ in different HV 57
4.20 Remained high frequency noise 57
4.21 Cut for select dark count from electronic noise 58
4.22 Effect of 70m co-axis signal cable 58

5.1 Single p.e. response of HPD with each HV module 61
5.2 HV cable 62
5.3 Effect on single p.e. response of 70m HV cable 63
5.4 Setup for On-Off resistant measurement 63

List of Tables

2.1 Comparison of the performance between an 20cm HPD (with a preamplifier with a gain of 100) and a 50 cm SK PMT. 22
2.2 Specification of the HV module 25
2.3 Specification of the preamplifier 26
2.4 Specification of the control power supply 26

3.1 The temperature dependence of the gain of the AD and that of the HPD (with preamplifier) at AD bias voltage of 300 V, 20 °C 30
3.2 Signal response of 50 cm HPD with 5mm AD 34
3.3 Performance of HPD with ϕ5 mm AD 42

4.1 Single photoelectron characteristics of 50 cm HPD w/ 5ch 20mm AD . . . 47
4.2 Effect of decoupling transformer on the multi photoelectron response of 50 cm HPD w/ ϕ14.7 mm AD 52
4.3 Single photoelectron of 50 cm HPD w/ 14.7mm AD and decoupling transformer 56
4.4 Dark count rate in different HV of 50 cm HPD with 14.7mm AD 57
4.5 Effect of 70m co-axis signal cable 58

5.1 Single p.e. response of HPD with each HV module 61
5.2 Specification of the HV cable 62
5.3 Effect on single p.e. response of 70m HV cable 62

Abbreviations

SK	**S**uper **K**amiokande
HK	**H**yper **K**amiokande
AD	**A**vlanche **D**iode
HPD	**H**ybrid **P**hoto **D**etector
PMT	**P**hoto**m**ultiplier **T**ube
TTS	**T**ransit **T**ime **S**pread
PD	**P**hoto **D**etector
TDC	**T**ime to **D**igital **C**onverter
p.e.	**p**hoton **e**lectron
QE	**Q**uantum **E**fficiency
HV	**H**igh **V**oltage
LV	**L**ow **V**oltage
FWHM	**F**ull **W**idth **H**alf **M**aximum

Chapter 1

Introduction

Currently the universe is matter dominated, while comparable amounts of matter and anti-matter were created in the Big-Bang. CP violation is believed to contribute to the asymmetry between matter and anti-matter, so that matter remains during the expansion and cooling process of the universe [5]. CP invariance is observed to be violated in weak interactions of quark sector [6], while CP violation in lepton sector is not observed yet. Neutrino oscillation provides a way to observe the CP violation in lepton sector. Moreover, observations showed that neutrino mixing angles are very different from those of quarks, which suggest that the mass ordering might not be as expected by the knowledge from the quark sector.

1.1 Neutrino Oscillation

Neutrinos are leptons which lack electric charge and are extremely difficult to be detected as they pass through ordinary matter almost without disturbance. There are three flavors of neutrinos observed, electron neutrino (ν_e), muon neutrino (ν_μ) and tau neutrino (ν_τ). They are assumed to be massless in the Standard Model of Particle Physics. However, neutrino oscillations have been observed in solar [7], atmospheric [8], accelerator [9] and reactor experiments [10, 11], which implies neutrino flavor eigenstates are actually made up of superposition of neutrino mass eigenstates [12], suggesting physics beyond the Standard Model.

Neutrino oscillation was proposed by Maki, Nakagawa, Sakata [13] and Pontecorvo [14]. The flavor eigenstates can be written as superposition of mass eigenstates:

$$|\nu_\alpha\rangle = \sum_{i=1}^{3} U_{\alpha i}|\nu_i\rangle \tag{1.1}$$

where $|\nu_\alpha\rangle$ is the flavor eigenstate ν_e, ν_μ or ν_τ, $|\nu_i\rangle$ is the mass eigenstates ν_1, ν_2 or ν_3. U is the Pontecorvo-Maki-Nakagawa-Sakata matrix which is a 3 × 3 matrix describing the transformation between different neutrino flavor eigenstates:

$$U = \begin{pmatrix} 1 & 0 & 0 \\ 0 & \cos\theta_{23} & \sin\theta_{23} \\ 0 & -\sin\theta_{23} & \cos\theta_{23} \end{pmatrix} \times \begin{pmatrix} \cos\theta_{13} & 0 & \sin\theta_{13}e^{-i\delta} \\ 0 & 1 & 0 \\ -\sin\theta_{13}e^{i\delta} & 0 & \cos\theta_{23} \end{pmatrix} \times \begin{pmatrix} \cos\theta_{12} & \sin\theta_{12} & 0 \\ -\sin\theta_{12} & \cos\theta_{12} & 0 \\ 0 & 0 & 1 \end{pmatrix} \tag{1.2}$$

The time evolution of the threes eigenstates is

$$\begin{aligned} |\nu_\alpha(t)\rangle &= \sum_i U_{\alpha i}e^{-iE_i t}|\nu_i(t=0)\rangle \\ &= \sum_i \sum_{\alpha'} U_{\alpha i}U^*_{\alpha' i}e^{-iE_i t}|\nu'_\alpha(t=0)\rangle \end{aligned} \tag{1.3}$$

where E_i is the eigenvalue of the mass eigenstate $|\nu_i\rangle$. The probability for flavor eigenstate ν_α at t = 0 to change to state ν_β at time t is:

$$\begin{aligned} P(\nu_\alpha \to \nu_\beta) &= |\langle\nu_\beta(t)|\nu_\alpha(0)\rangle|^2 \\ &= |\sum_i U_{\beta i}U^*_{\alpha i}e^{-iE_i t}|^2 \\ &= \sum_i |U_{\alpha i}U_{\beta i}|^2 + \sum_{i\neq j} U_{\alpha i}U^*_{\beta i}U^*_{\alpha j}U_{\beta j}e^{-i(E_i-E_j)t} \end{aligned} \tag{1.4}$$

The above equation shows that the flavor transition phenomenon, neutrino oscillation, occurs due to the mixing of the mass eigenstate of the non-zero-mass neutrinos.

The mixing matrix U can be simplified in the case of the two-flavor mixing:

$$U = \begin{pmatrix} \cos\theta & \sin\theta \\ -\sin\theta & \cos\theta \end{pmatrix} \tag{1.5}$$

Transition probability shown in (1.4) can be simplified into:

$$P(\nu_\alpha \to \nu_\beta) = \sin^2 2\theta \sin^2(\frac{(E_i - E_j)t}{2}) \tag{1.6}$$

If neutrinos have non-zero mass, the follow approximation can be taken:

$$\begin{aligned} E_i - E_j &= \sqrt{(m_i^2 + p_i^2)} - \sqrt{(m_j^2 + p_j^2)} \\ &= p_i(1 + \frac{m_i^2}{p_i^2})^{\frac{1}{2}} - p_j(1 + \frac{m_i^2}{p_j^2})^{\frac{1}{2}} \\ &\approx (p + \frac{m_i^2}{2p}) - (p + \frac{m_j^2}{2p}) \\ &\approx \frac{\Delta m_{ij}^2}{2E} \end{aligned} \tag{1.7}$$

where $\Delta m_{ij}^2 \equiv m_i^2 - m_j^2$ is the mass-squared difference of the neutrino mass eigenstates. Substituting equation (1.7) into equation (1.6), with neutrino flight length L_ν and neutrino energy E_ν, the survival probability of ν_α in two-flavor mixing case is:

$$\begin{aligned} P(\nu_\alpha \to \nu_\alpha) &= 1 - P(\nu_\alpha \to \nu_\beta) \\ &= 1 - \sin^2 2\theta \sin^2(\frac{\Delta m_{ij}^2 L_\nu}{4E_\nu}) \\ &= 1 - \sin^2 2\theta \sin^2(\frac{1.27 \Delta m_{ij}^2(\mathrm{eV}^2) L_\nu(\mathrm{km})}{E_\nu(\mathrm{GeV})}) \end{aligned} \tag{1.8}$$

As shown above, the oscillation probability depends on the mixing angle θ, the mass square difference Δm_{ij}^2, neutrino flight length L_ν and neutrino energy E_ν. The oscillation amplitude is at maximum when

$$\frac{L_\nu(\mathrm{km})}{E_\nu(\mathrm{GeV})} \sim \frac{\pi}{2.54 \times \Delta m_{ij}^2(\mathrm{eV})} \tag{1.9}$$

Therefore, neutrino oscillation experiments can probe the neutrino squared mass difference.

1.2 Mass hierarchy & Leptonic CP violation

Now, almost all of the parameters of the neutrino oscillation are known except the sign of Δm_{23}^2 and the CP phase δ. The first one called mass hierarchy problem and the latter one is related to the CP violation in lepton section.

The mass hierarchy is not yet known because neutrino oscillation experiments are measuring the mass differences (Δm^2_{12} and Δm^2_{23}) instead of the absolute mass (Eq. 1.8). With $m_3 \gg m_2 > m_1$, it is defined as normal hierarchy, while with $m_2 > m_1 \gg m_3$, it is defined as inverted hierarchy. A way to determine the mass hierarchy of neutrino is to observe the sub-dominant effect of the neutrino oscillation. For example, the atmospheric neutrino oscillation observed by Super-K experiment, matter effect plays an important role in these oscillation schemes. When the atmospheric neutrinos traverse the Earth, the Earth's matter potential due to the forward scattering amplitude of charged current ν_e and $\bar{\nu}_e$ interactions with electrons has to be taken into account. The Earth contains a large number of electrons, ν_e interacts with these electrons via W bosons while ν_μ and ν_τ do not. For normal hierarchy (inverted hierarchy), the possibility of ν_e ($\bar{\nu}_e$) appearance will be enhanced by Mikheyev-Smirnov-Wolfenstein resonant [15, 16]. By observing the difference of the appearance possibility, the mass hierarchy can be determined, which can also help to measure the CP phase.

The effect of the CP phase appears in the difference between the transition probabilities $P(\nu_\alpha \rightarrow \nu_\beta)$ and $P(\bar{\nu}_\alpha \rightarrow \bar{\nu}_\beta)$. We have an opportunity to measure the δ thanks to the large angle of θ_{13}. The most promising channel to detect the difference in transition probabilities is $\nu_\mu(\bar{\nu}_\mu) \rightarrow \nu_e(\bar{\nu}_e)$. Accelerator-based neutrino oscillation experiment, such as T2K (Tokai to Kamioka) experiment and NOvA (NuMI Off-Axis ν_e Appearance) experiment, can measure these two channels. For T2K, the ν_μ beam or the $\bar{\nu}_\mu$ beam is generated by the J-PARC accelerator located in Tokai-mura, and then detected by the near detector, ND280, and the far detector, Super-Kamiokande detector, which is 295km far from the J-PARC accelerator. By comparison of the neutrino flux between two detectors, the oscillation probability in these two channels can be extracted. T2K is expected to have sensitivity to the CP phase δ_{CP} at 90% confidence level (C.L.) or higher over a significant range. For example, if $\sin^2\theta_{23}$ is maximal, $-115^\circ < \delta_{CP} < -60^\circ$ for normal hierarchy and $50^\circ < \delta_{CP} < 130^\circ$ for invert hierarchy [17].

To determine the mass hierarchy and CP phase, more statistics of neutrino and anti-neutrino events is needed, which means that a larger detector than Super-Kamiokande and higher intensity neutrino beam are strongly required.

1.3 Neutrino detection

Because the neutrino is chargeless, we can only detect the presence of a neutrino in our experiment if it interacts. There are two kinds of interactions:

- Charged-current interactions

  The neutrino converts into the equivalent charged lepton (e.g. inverse beta decay, $\nu_e + p \rightarrow n + e^+$). The neutrino is detected via the detection of these charged lepton. The flavor of the neutrino (e.g. e, μ, τ) is also can be determined. The reason to call this kind of interactions is because that it occurs through the exchange of a $W^{\pm}$.

- Neutral-current interactions

  There are only energy and momentum exchange between the neutrino and the target. After interaction, the neutrino remains a neutrino. By observing the target recoils (e.g. neutrino-electron scattering, $\nu + e \rightarrow \nu + e$) or the secondary particle from the broken target (e.g. ${}^2H + \nu \rightarrow p + n + \nu$), the neutrino can be detected but its type is unknown. This kind of interactions occurs through the exchange of a Z^0.

Furthermore, for both of charged-current interactions and neutral-current interactions, the neutrino interactions can also be categorized according to the product of interaction as follows [18].

- quasi-elastic scattering ($\nu + N \rightarrow l + N'$)
- single meson production via baryon resonances ($\nu + N \rightarrow l + N' + m$)
- coherent pion production ($\nu + A \rightarrow l + \pi + A$)
- deep inelastic scattering ($\nu + N \rightarrow l + N' + hadrons$)

where N and N' are nucleons (proton or neutron) which can be either free or inside nucleus, l is a lepton, m is a meson and A is a nucleus. For the quasi-elastic scattering, the kinematics parameters of neutrino can be calculated according to the energy and momentum of the charged particle(s) measured by detector,

1.3.1 Principle of Water-Cherenkov detector

It is known that when a charged particle travels faster than light in the medium, a kind of shock wave, known as Cherenkov light will be generated and forms a cone shape alongside the moving charged particle. The angle (θ) between the direction of the traveling charged particle and the Cherenkov light, which is called the Cherenkov angle, is determined by the velocity of the charged particle and that of the light in the medium.

$$\cos\theta = \frac{1}{n \times \beta}(\beta \equiv \frac{v}{c}) \tag{1.10}$$

For example, when a muon travels in water at quasi light speed and the refractive index of water (n=1.33) is substituted, the angle is calculated to be $\sim$ 41 degrees. Fig 1.1 illustrates the inside of the water tank and the traveling charged particle as it emits Cherenkov light.

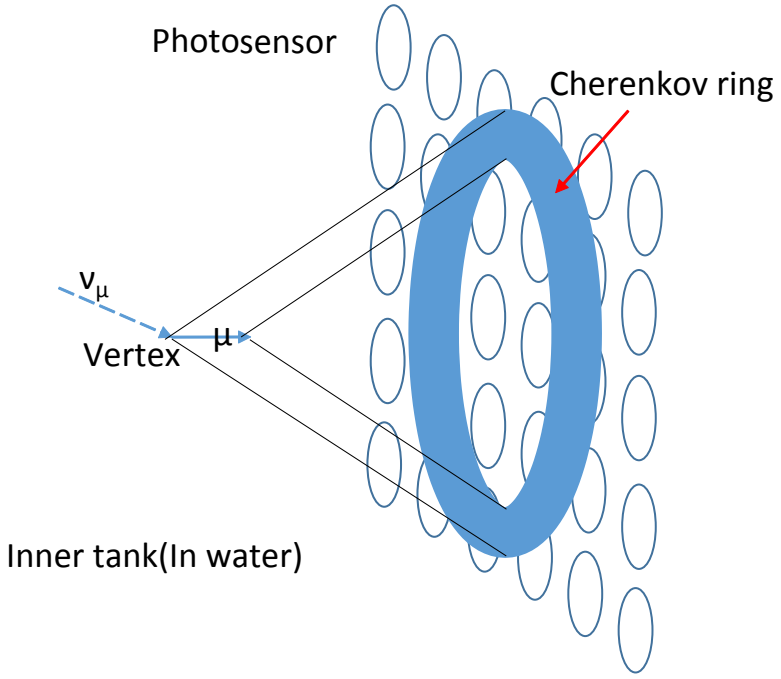

FIGURE 1.1: Image of a charged particle emitting Cherenkov light

As shown in Fig. 1.1, Cherenkov light forms a cone shape from the vertex point as it expands toward the inner wall of the water tank. The number of photons (N) emitted per unit wavelength (λ), and unit traveling distance (x) of the charged muon particle is expressed by equation 1.11. Here, α is the fine structure constant ($\sim 1/137$).

$$\frac{d^2N}{dxd\lambda} = 2\pi\alpha(1 - \frac{1}{n^2\beta^2})\frac{1}{\lambda^2} = 2\pi\alpha\sin^2\theta\frac{1}{\lambda^2} \tag{1.11}$$

From Eq. 1.10 and Eq. 1.11, we can see that the Cherenkov angle becomes smaller as the charged particle loses its kinetic energy, leading to a reduction in the number of photons emitted. When the charged muon particle stops inside the water tank, the Cherenkov light projected to the inner wall forms a donut shaped image called the Cherenkov ring (Fig 1.1). The charged particle is detected by sensing the Cherenkov light with PMTs installed on the wall. Each PMT hit by Cherenkov light converts the light signal into the charge signal that corresponds to the signal intensity and then sends it to the DAQ system. The ring image is reconstructed off-line by computing the timing and intensity information of each signal sent by PMTs. The vertex point, event time, direction, type and energy of the charged particle and neutrino can then be determined by reconstruction.

1.3.2 Water-Cherenkov detector in neutrino physics experiment

For the long baseline neutrino oscillation experiments which use an artificial neutrino beam, the occurrence of neutrino oscillation is examined by comparing the neutrino beam flux before and after traveling a certain distance. Therefore, two detectors, including the near detector and the far detector are required to do this comparison. In the T2K experiment, a complex detector called ND280 is used as the near detector and the Super-Kamiokande detector is used at the far detector (Fig. 1.2).

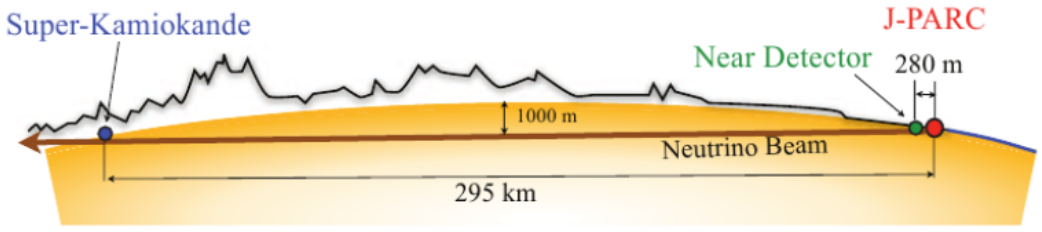

FIGURE 1.2: T2K experiment

Super-Kamiokande is a cylindrical 50 kton water Cherenkov detector. Fig. 1.3 shows the schematic view of the detector and its location in Mountain Ikenoyama. The detector is located in a zinc mine under the top of Mountain Ikenoyama which has a mean rock overburden of ∼1000m (∼ 2700m water equivalent). A total number of $\sim 11,200$ of 50 cm photomultiplier tubes (PMTs) are installed facing toward the center of the tank (Fig.

1.4). The PMTs detect the Cherenkov lights which are generated by charged particles that result from the interactions between a nucleon in water and an incoming neutrino.

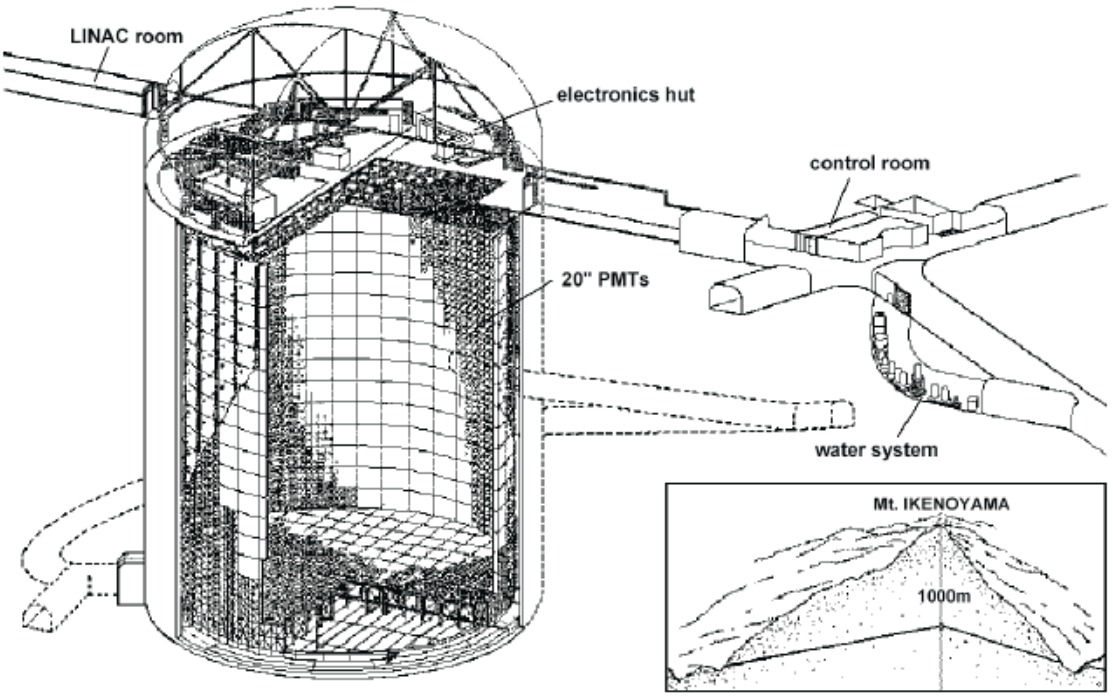

FIGURE 1.3: Super Kamiokande detector

1.4 Hyper-Kamiokande project

Hyper-Kamiokande (Hyper-K) is a proposed next generation underground water Cherenkov detector capable of observing leptonic CP violation, nucleon decay, supernova neutrino and so on. It has 0.99(0.56) Mt total (fiducial) mass, which is about 20(25) times larger than that of Super-Kamioande (Fig. 1.5)[19, 20]. The candidate site is Kamioka mine, Gifu, Japan because it is easy to get pure water and bedrocks is hard there. Fig. 1.6 shows a cross section of Hyper-K tank, which consists of inner detector and outer detector[19]. In the baseline design, about 99,000 50 cm photosensors (25,000 20cm photosensors) are needed for inner detector (outer detector). The photo-coverage, which indicates the photosensitive area in the inner tank is 20%, half of that of Super-K.

One of the main physics topics of Hyper-K is the neutrino oscillation, as has been stated in Section 1.1 and Section 1.2. Based on the full MC simulation with latest systematic uncertainties used in the current Super-Kamiokande analyses, it has been found that

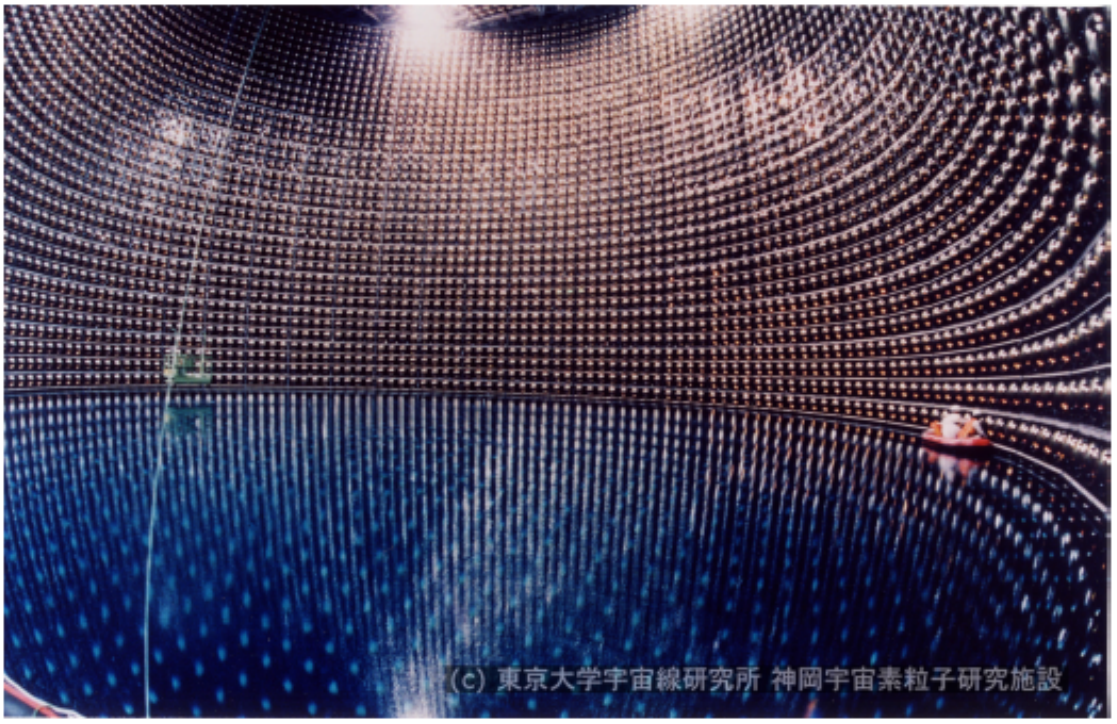

FIGURE 1.4: Internal view of the tank of the Super Kamiokande detector

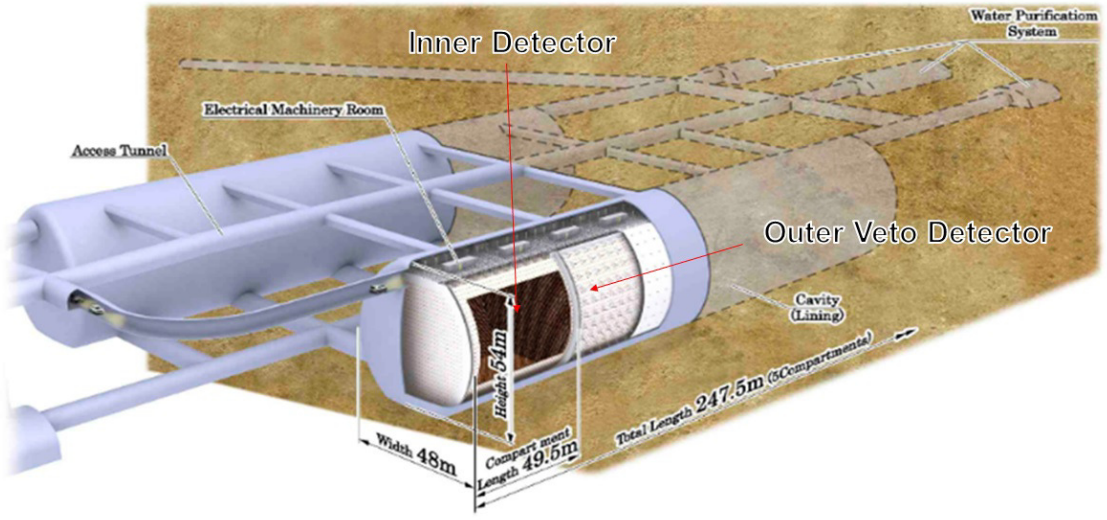

FIGURE 1.5: Hyper-Kamiokande detecotr

the expected significance for the mass hierarchy determination is more than 3σ provided $\sin 2\theta_{23} > 0.4$. We expect to be able to discriminate between $\sin 2\theta_{23} < 0.5$ (first octant) and > 0.5 (second octant) if $\sin^2 2\theta_{23}$ is less than 0.99. For the CP violation phase in lepton sector, assuming the mass hierarchy is determined by other means and that the total systematic error managed to the 5% level then the CP phase may be distinguished from $\delta = 0$ at 3σ for 74% of the entire range in σ [21].

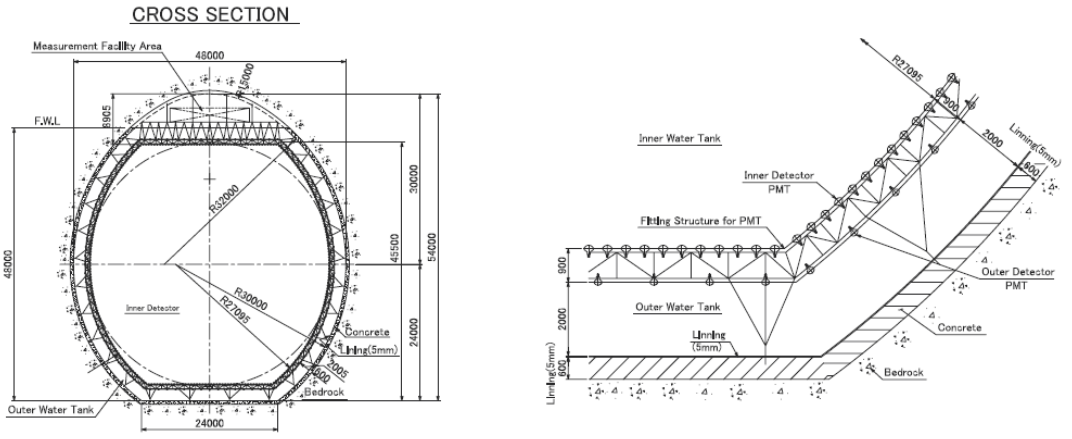

FIGURE 1.6: Cross section of Hyper-Kamiokande detector

1.5 Other physics topics of Hyper-Kamioaknde

1.5.1 Nucleon decay

Grand Unified Theories (GUTs) are proposed as a candidate of a framework beyond the standard model. GUTs unify the strong and electroweak forces. Most of GUTs allow baryon number violating interactions and thus predicts the nucleon decays.

Super-Kamiokande searches for the nucleon decays such as $p \to e^+ + \pi^0$ and $p \to \bar{\nu} K^+$ since 1996. Super-K is the largest detector for the observation of nucleon decay in the world. No nucleon decay candidate event has been detected until now. The current limit of proton partial lifetime is 5.9×10^{33} years for $p \to \bar{\nu} + K^+$ [22].

One of GUTs, SUSY SO(10), predicts that the limit of proton lifetime is the order of 10^{35} years. If the proton lifetime is shorter than 5.7×10^{34} years for the $p \to e^+ \pi^0$ mode, or shorter than 1.0×10^{34} years for$p \to \bar{\nu} K^+$, Hyper-K experiment has a sensitivity which could discover a signal over the atmospheric neutrino background events with a 3σ significance by collecting a 5.6 Megaton·year exposure [19].

1.5.2 Astrophysics using neutrinos

The supernova, which is a stellar explosion at the end of a massive star, will emit many neutrinos called the supernova burst neutrinos. The energy of the supernova burst neutrinos is expected to be about $10 \sim 30$ MeV. The observation of the supernova burst

neutrinos gives us a clue to explore the mechanism of the supernova explosion. On 23. Feb. 1987, the Kamiokande II [23], IMB [24] and Baksan [25] experiments observed the supernova burst neutrinos from SN1987A located in the Large Magellanic Cloud. Neutrino astronomy starts from this discovery. Recently, it is said that Betelgeuse(197 ± 45 pc) and and VY Canis Majoris ($\sim$1.5 kpc) might explode and emit the supernova neutrinos [26]. Quite high statistical observations of supernova neutrinos are expected for galactic supernovae (e.g. 170,000$\sim$260,000 events for a 10 kpc supernova), Hyper-K will give us the detailed time profile and temperature variation during the burst [19].

The neutrino from the sun produced by the process of nuclear fusion is called the solar neutrino. The energy of the solar neutrinos is often below 20MeV. By observing the solar neutrinos, we can study the internal state of the sun in real time. The standard solar model can be verified by the observation of the solar neutrinos. Hyper-K will provide short time and high precision variability analyses of the solar core activity. The solar core temperature could be monitored within a few percent accuracy day by day, and to a tenth of a percent over the period of several months [19].

Chapter 2

Development of new photo-detector for Hyper-K

2.1 Requirements for the photosensor in Hyper-K

The role of the photosensor is to detect the Cherenkov light that result from rarely occurring neutrino interactions and then send the precise timing and energy information of the detected light. For Hyper-K, a photosensor should satisfy the following requirements.

- High single photon detection efficiency
- Good single photon energy resolution
- Good single photon timing resolution
- Low dark count rate
- Good linearity and wide dynamic range
- High rate tolerance
- Low production cost
- Long lifetime and good stability

In this chapter, the requirements listed above shall be discussed in detail.

2.1.1 Single photon detection efficiency

As mentioned in Section 1.3.1, the intensity of incident Cherenkov lights on a photosensor is weak: quite often as weak as a single photon level under an energy of 10MeV neutrino interaction [27]. And since the neutrino event itself very rarely occurs, the sensor must be sure to detect each and every event. Furthermore, the photo-coverage in the inner tank of Hyper-K is only half of that of Super-K. A photosensor with higher single photon detection efficiency is important to Hyper-K detector.

The single photon detection efficiency of PMT is generally determined by three factors as following. [28]

1. Photocathode quantum efficiency
2. Photoelectron collection efficiency at the first dynode
3. Trigger efficiency

As for Factor # 1, quantum efficiency of the bialkali photocathode PMT used in the Super-Kamiokande detector is $\sim$ 22% at a Cherenkov light wavelength of $\sim$ 390 nm. Currently, the dominant factor that limits the detection efficiency is the quantum efficiency of the photocathode: other two factors can reach about $\sim$ 80%. The latest photocathode activation technique has recently enabled the same kind of photocathode to achieve about 1.4 times higher quantum efficiency (Section 2.3).

For factor #2, the collection efficiency is approximately 73% for the Super-Kamiokande PMT [27]. This collection efficiency limitation is derived from the Venetian blind dynode structure of the current PMT. The cause of the loss is that some photoelectrons from the photocathode do not hit the first dynode and therefore do not yield secondary electrons at the dynodes.

Factor #3 depends on the readout electronics noise level and variation of PMT output pulse height distribution in response to the single photon signals. In the current Super-Kamiokande system, the threshold level of the readout electronics is set at 1/4 photon electron (p.e.). equivalent signal intensity[29] (Fig. 2.1). If a lower noise level can be achieved, the threshold level can be set lower so that the trigger efficiency would rise.

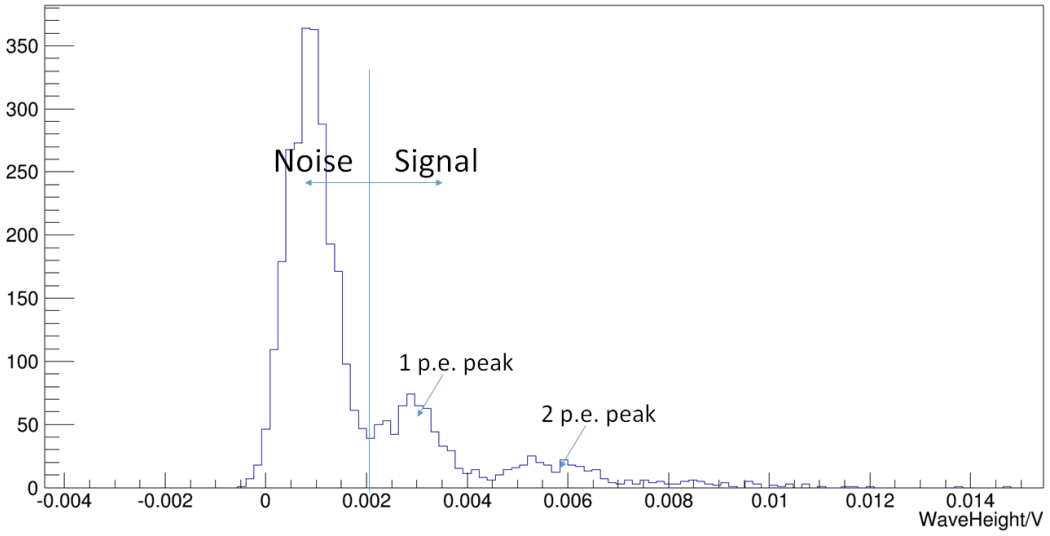

FIGURE 2.1: Photon electron response pulse height distribution of a 50 cm HPD prototype

Among these factors which can influence the detection efficiency, the first factor is only influenced by the material used by cathode and the wavelength of the incident light; the second factor, collection efficiency can be improved by using new cathode structure and optimization on the electronic field in the vacuum tube; and finally, the trigger efficiency can be improved by optimization of the read out electronics for the reduction of noise level. For the development of new kind of photosensor, all of these three factors are considered.

2.1.2 Single photon energy resolution

Single photon energy resolution is often expressed by Eq. 2.1.

$$R = \frac{\sigma}{\mu} \times 100\% \tag{2.1}$$

Here, σ is the standard deviation of the output signal pulse height of single photon and μ is the single p.e. peak value of output pulse height distribution. (Fig. 2.1)

It is easy to image that the a clearer separation of the noise and signal would be possible and as a result a smaller signal loss if the energy resolution is higher, in other words, the pulse height distribution is narrower. As a result, a higher trigger efficiency, as mentioned in the section 2.1.1 can be obtained. Thus, gaining a better single photon

energy resolution is an effective approach to improve the detection efficiency of the photosensor. For the PMT with conventional structure, such as Super-Kamiokande PMT, the energy resolution, R is mainly determined by the gain of the first stage of the secondary-electron multiplier section (first dynode), δ_1.

$$R \propto \frac{1}{\sqrt{\delta_1}} \tag{2.2}$$

Fig 2.2 plots the gain of the first dynode for several kinds of dynode materials as a function of applied voltage between the photocathode and the first dynode [3]. The value of δ_1 increases with voltage applied, but all of them have saturation point. The GaP type dynode seems good but in reality, the complex manufacturing process makes it cannot be used commonly.

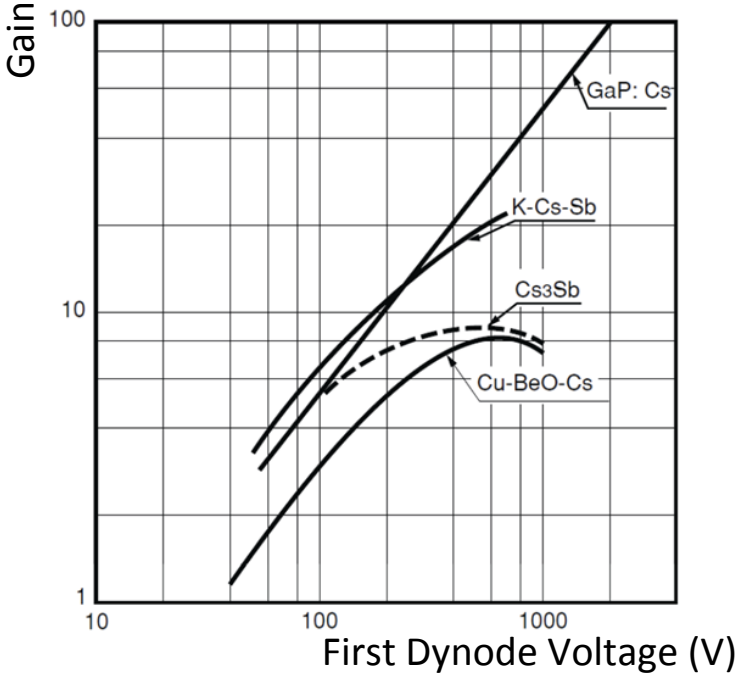

FIGURE 2.2: First stage gain as a function of the accelerating voltage [3]

Accordingly, there is a clear limit of achievable first secondary electron gain in the current PMT electron multiplication structure. The application of avalanche diode, which will be introduced in Section 2.5.1, with a higher accelerating voltage can be expected to get a higher single photon energy resolution than that of conventional PMT.

2.1.3 Single photon timing resolution

The interaction vertex is reconstructed based on the reconstructed Cherenkov ring image and the timing information of the Cherenkov light arriving at each photosensor. Accordingly, accuracy of the vertex point determination depends largely on the timing resolution of the photosensor and therefore the timing jitter of the photosensor should be as small as possible.

Furthermore, the sensitivity to some kinds of events with high time resolution requirement, such as the $p \to \bar{\nu}K^{+}\gamma$ event, will be improved for a detector with better time resolution. The proton decay event in this channel can be selected by searching hit cluster made by 6MeV γ before μ. A photosensor with better time resolution can make us select the γ from the dark rate and other backgrounds with higher precision.

However, even if it were possible to make the timing jitter of the photosensor, including the spread of transit time from photocathode to anode and the variation of the transit time with the incident point, zero, the time resolution of photosensor is not zero because of the different light path[28]. If one photosensor detects photons originating at the same vertex point but not along the same travel path, the time of detection (Fig 2.3) would also be different. The limit of the time resolution σ_{lim} due to the different travel path can be estimated by

$$\sigma_{lim} \sim \frac{D}{c'} \tag{2.3}$$

Here, D represents the diameter of photocathode of the photosensor and c' is the speed of light in the water (~ 0.23 m/ns). When a photosensor with a photocathode diameter size of 0.5m is used, σ_{lim} is estimated to be $\sim$2.2 ns. As a result, it is enough for that the timing resolution of the photosensor itself is smaller than 2.2ns.

The time jitter of the PMT is determined by two components (2.4): one is the time jitter occurring when the photoelectrons travel between photocathode and the first stage of the dynode (σ_{pc_em}), the other is the time jitter during the electron multiplication process (σ_{em}).

$$\sigma^2_{PMT} = \sigma^2_{pc_em} + \sigma^2_{em} \tag{2.4}$$

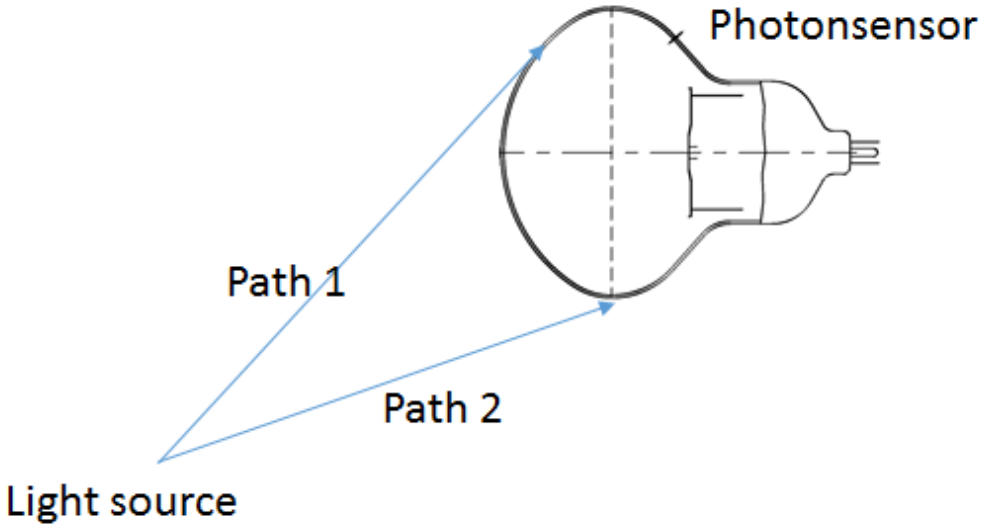

FIGURE 2.3: The time difference due to different light path

The first item is dominated by the accelerate voltage: a higher accelerate voltage brings a smaller time variation because the photoelectrons can travel faster between photocathode and the first stage of the dynode. For the second item, it is determined by the structure of cathode, or dynode for PMT. The time jitter during the electron multiplication process can be smaller if the distance of the photoelectron drift path in dynode is more similar. Furthermore, the second item can be ignored for some other multiplication mechanism, such as avalanche multiplication.

2.1.4 Dark count rate

Any PMT will yield fake single photon level signals even being operated in complete darkness. These signals are called dark count and are caused by thermal electron emission from the photocathode. The rate of the dark pulse depends on the photocathode material, the size of the photocathode area, the collection efficiency and the ambient temperature.

A lower dark rate is desired because it can bring a lower trigger threshold and thus a higher trigger efficiency. Furthermore, for the detection of low energy events, a lower dark rate could give us better sensitivity. For example, the decay channel of $p \to \nu k^+ \gamma$: $K^+ \to \mu^+ \nu$, the energy of the γ released by the proton is only 6MeV, which means that there would be only about several tens of hits on PMTs [22]. If the dark count rate was

high, the S/N is in a given measurement time window would be decreased, thus it would be hard to distinguish whether the hit is from the γ signal or the dark count.

For the PMT used in Super-K, the dark count rate is about 4.2 kHz during operation. Considering more photosensors will be used, a low dark count rate of the photosensor is more important for Hyper-K. The exact requirement has not been decided yet. Its effect on the trigger efficiency and the physics is under study.

2.1.5 Linearity and wide dynamic range

As has been stated in Chapter 1, the physics targets of Hyper-K are very wide, including the measurement of CP violation phase in lepton sector, the determination of the mass hierarchy of neutrinos, the search of nucleon decay and some other topics about the astrophysics. As a result, the Hyper-K detector need to observe the events in a wide dynamic range: from several MeV (e.g. solar neutrino, supernova neutrino) to several GeV (atmospheric neutrino, accelerator neutrino). For the photosensor in Hyper-K, the number of photoelectron which can be detected is required from 1p.e. to 1,000 p.e.

The linearity of a PMT is influenced by two factors.

- Cathode linearity
- Anode linearity

For the cathode, or the photocathode in PMT, many photoelectron will be generated, in other words, the current would be high in high luminosity, then the voltage between the cathode and anode would be changed because of the resistance of the cathode. As a result, the cathode linearity is dominated by the material used.

For the anode, or the dynode in PMT, its linearity is limited by two factors: the voltage-divider and space charge effects in the dynodes. In high luminosity, the number of photoelectron in the dynode is very large. The potential of each stage of the dynode would be changed, not the same as the designed value of the potential, because of the large signal current. Furthermore, so many photoelectron might change the electronic field between the stages of the dynodes. These two factors limit the linearity and dynamic range of PMT.

2.1.6 Other important characteristics

As has been stated at the start of this section, there are other important characteristics for the photosensor for Hyper-K.

- Rate tolerance

  For the supernova explosion, the photon-sensor might detect a large number of events in a short time. The sensor needs to be capable of handling high rate signal up to 1 MHz.

- Production cost

  About 100, 000 photosensors, 9 times of the number of photosensors used in Super-K, will be used in Hyper-K. The reduction of the production cost is important. A way to reduce the production is to simplify the structure of the photosensor, especially the anode part.

- Lifetime and stability

  The Hyper-K is proposed to operate more than 10 years. Moreover, the number of photosensors used in Hyper-K is very large. As a result, a photosensor with long lifetime and good stability can make the Hyper-K detector operate stably.

2.2 Candidates of new Photosensor

There are three candidates for photosensors in Hyper-Kamiokande as follows

- Venetian Blind dynode type PMT (SK PMT)

  It is employed in SK. The performance is well confirmed.

- Box & Line PMT(B&L PMT)

  It is a new type of PMT. which has better timing resolution and energy resolution than SK PMT.

- Hybrid photon detector (HPD)

  It uses an avalanche diode instead of dynode to multiply the photo-electrons. The development of HPD is the main topic of this thesis.

Figure 2.4 shows the drawings of three candidates. The major difference between HPD and PMT is that the multiplication structure in HPD is an avalanche diode rather than the dynode which is used by PMT. Therefore HPD has a much simpler structure, a better timing resolution and a better resolution of single photoelectron than PMT.

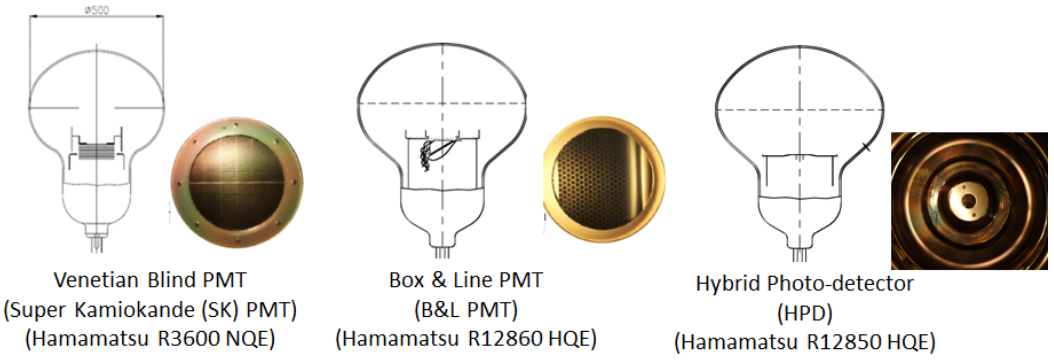

FIGURE 2.4: Three candidates of the photo-sensors for Hyper-K (provided by Hamamatsu)

2.3 High-QE photocathode development

A high-QE version of SK PMT, which has 30% at maximum, 1.4 times larger than that of normal SK PMT, has been developed by Hamamatsu Photonics K.K.. The QE spectra as a function of wavelength for eight high-QE version SK PMT and a typical value of normal-QE PMTs are shown in Fig 2.5. The high-QE technique is also been applied to other candidates of Hyper-K photosensor.

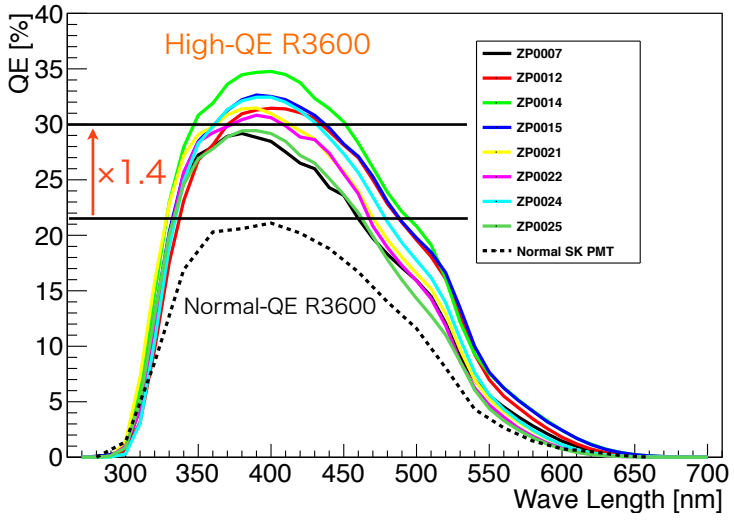

FIGURE 2.5: Comparison on QE between High QE version PMT and Normal QE version PMT (provided by Hamamatsu)

2.4 Schedule of development

Fig 2.6 shows the schedule of R&D of photosensors for Hyper-K. All of the three candidates, SK PMT, B&L PMT and HPD need to be evaluated and tested carefully and fully as following steps

1. Evaluate the basic performance, including single p.e. response, transit time spread, dark count rate and so on
2. Test the usability for Hyper-K in a 200-ton water Cherenkov detector
3. Detailed performance evaluation is carried out in parallel, including uniformity, linearity and so on

We plan to decide the photosensors for Hyper-K in Sep. 2016.

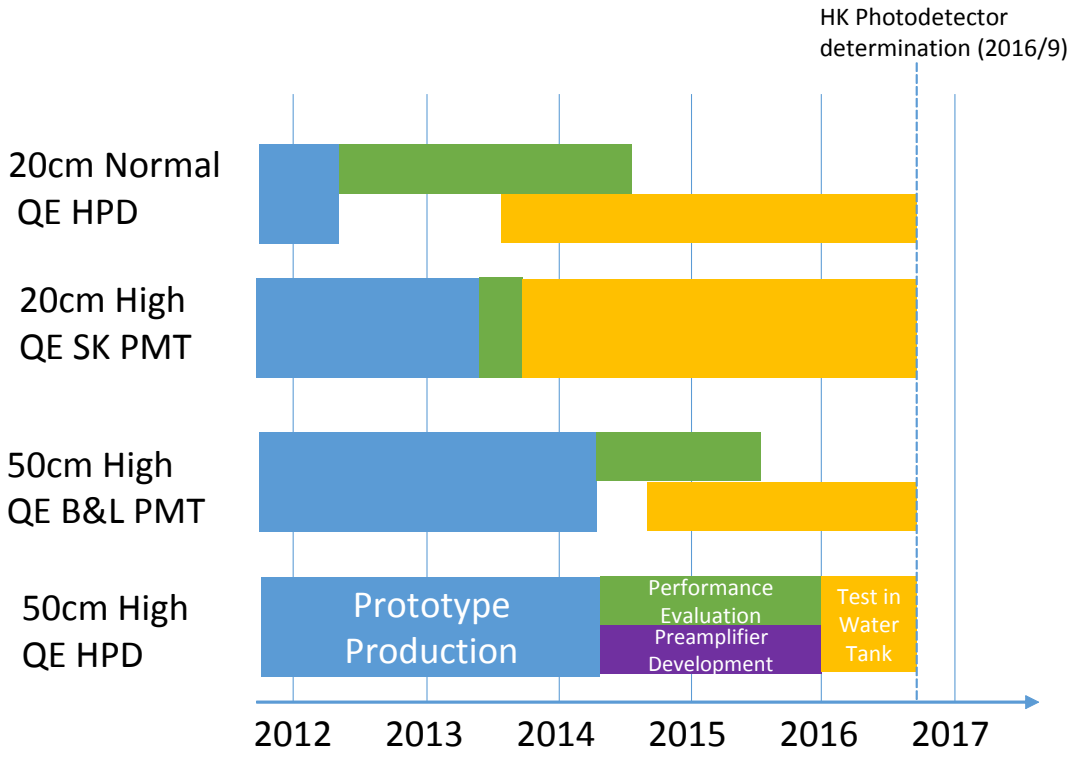

FIGURE 2.6: Development schedule of photon sensor for Hyper-Kamiokande

2.5 Hybrid Photo-Detector

The HPD is a hybridization of a vacuum tube and an avalanche diode (AD). The amplification system consists of two steps: a bombardment, which is caused by the high voltage

electric field between the photocathode and the surface of an AD, and an avalanche in the AD via a bias voltage (Fig. 2.7). In the case of an 20cm prototype HPD, the total gain is approximately 10^5, including the bombardment gain (∼1600 with a voltage of 8 kV), and the avalanche gain (∼100 with a bias voltage of 300 V). Although a preamplifier is required to achieve the same signal level as the PMT due to the smaller gain than that of the PMT (∼10^7), the advantage of the HPD is the better single photon resolution than that of the PMT because of a larger initial bombardment gain.

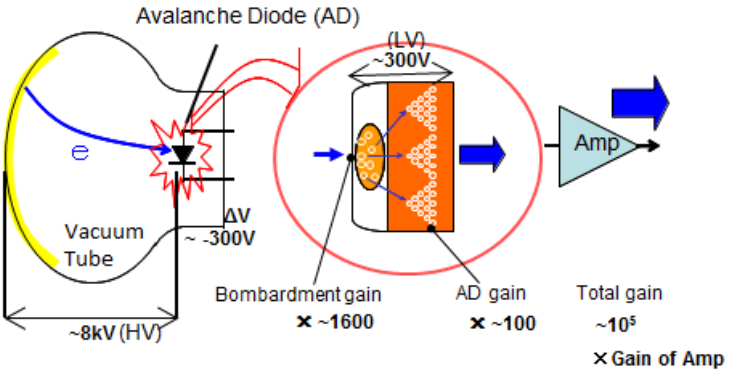

FIGURE 2.7: Principle of an HPD amplification and typical values of the 20cm HPD.

As a first step, we have developed a prototype of the 20cm HPD and measured its performance at the room temperature (Table 2.1).

TABLE 2.1: Comparison of the performance between an 20cm HPD (with a preamplifier with a gain of 100) and a 50 cm SK PMT.

	HPD	Super-K PMT [1]
Gain	1.5×10^7	∼10^7
Single p.e. Res. *	∼30%	∼60%
Dark Rate **	1 kHz	∼4 kHz
Peak/Valley ***	4.4	1.9

*: Abbreviation of the single photoelectron charge resolution. Sect. 3.1.3.
**: The threshold for the HPD (SK-PMT) is 0.5 p.e. (0.25 p.e.).
***: The definition would be introduced in Sect. 3.1.4.

2.5.1 Principle of avalanche diode

An avalanche diode (AD) is a semiconductor electronic device. By applying a high reverse bias voltage (typically several hundreds of Volts in silicon), the AD shows an internal current gain effect (around 100) due to impact ionization.

In the HPD, the photoelectron, which is generated by the photocathode of HPD will be accelerated by the high voltage between photocathode and get incident into the AD. The incident photoelectron will be accelerated by the electronic field, which is provided by the high reverse bias voltage. In the accelerating process, the incident photoelectron might knock other electrons free, creating free-electron-hole pairs (i.e. more charge carriers) and increasing the current. By measurement of these current, we can detect the incident electron.

On the other hand, the valence electron in a reverse-biased diode also may break free due to its thermal energy, creating an electron-hole pair. The electron will move towards the positive voltage while the hole will "move" towards the negative voltage due to the reverse bias voltage. If the voltage is high enough, the electron-hole pair also can knock other electrons free and creating more free-electron hole pairs, as the incident photoelectron. This is the reason of the leak current, a source of the noise, in the AD.

According to its multiplication principle, the AD has temperature dependency. When the temperature of AD increased, the valence electron would have more thermal energy and be easier to break free, then the leak current would be increased.On the other hand, the lattice vibration of the AD would be stronger. Therefore, the energy loss due to the collision between the electron and the phonon would become larger, which means that the energy can be used to ionized other valence electron would become small. As a result, the gain of AD is decreased [30]. The experimental result of the temperature dependency of the AD and the HPD is described in Section 3.1.

2.6 HPD system used in this thesis

The HPD used for the study described in this thesis is equipped with a preamplifier and a high voltage (HV) module as shown in Fig 2.8. Fig 2.9 shows pictures of an 20cm HPD without any accessories. A picture of the ϕ5 mm AD which is used in 20cm HPD is shown in Fig 2.10.

Fig 2.11 shows a schematic diagram of the circuit inside an HPD. The HV module produces two voltages: one is the high voltage applied between the photocathode and the AD, the other is the bias voltage of the AD. Usually, we apply the HV 8kV and the AD bias voltage around 300V (400V) for ϕ5 mm AD (ϕ20 mm AD). The specification of

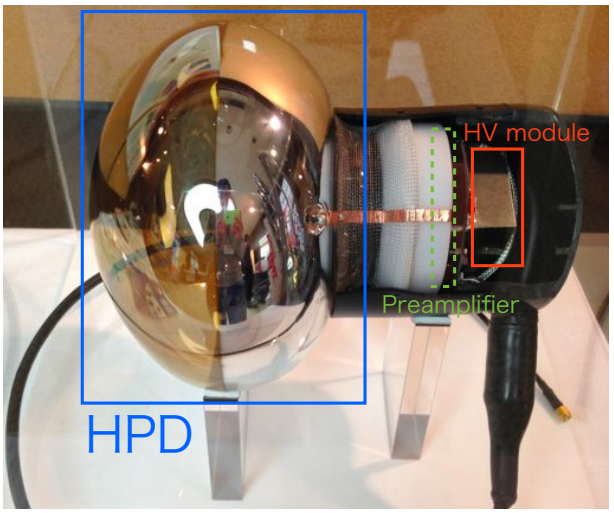

FIGURE 2.8: 20cm HPD

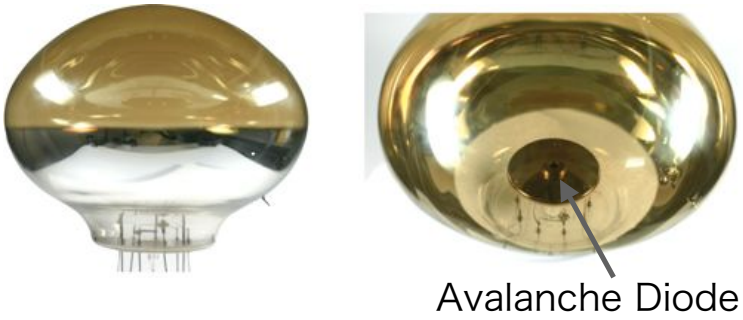

FIGURE 2.9: 20cm HPD without any accessories

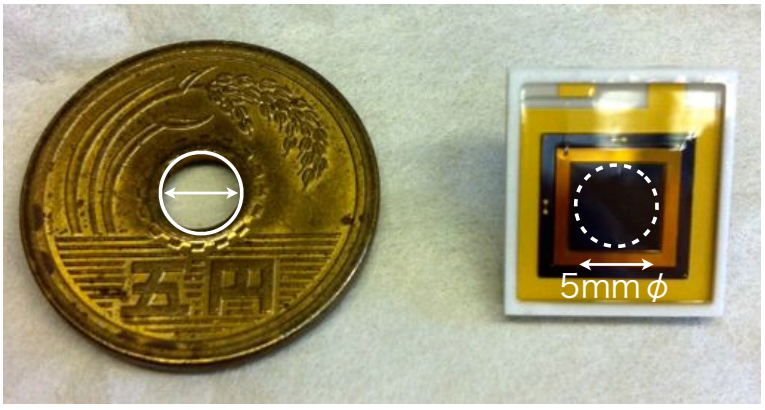

FIGURE 2.10: 5mm AD

the HV module is shown in Table 2.2. A low pass filter is put between the AD and the HV module to eliminate high frequency noise generated by the HV module. An inverted trans-impedance (Table 2.3) amplifier is used as the preamplifier to get enough gain and improve the S/N ratio. The reason of invert is just convenient to evaluate HPDs with other PMTs, which have minus signal. Two decoupling capacitor, one of them

for cathode and the other one for anode, are used to isolate the preamplifier part from the AD part, which has a high voltage of 8kV approximately. In order to protect the electronics from electric discharge, a varistor is placed next to the decoupling capacitor.

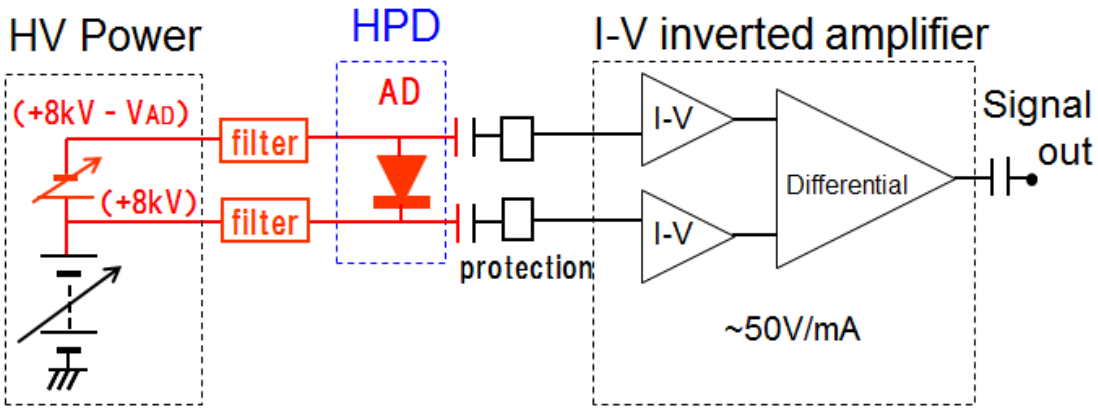

FIGURE 2.11: The schematic view of the circuit in the HPD

A control power supply shown in Fig 2.12 is used to control the HV and the AD bias voltage. It has four functions as following:

- Provide 10V for HV module
- Provide and control the HV control voltage and AD bias control voltage
- Monitor the over current status of the HV module
- Transmission of the signal from HPD to the DAQ system

The specification of the control power supply is shown in Table 2.4.

TABLE 2.2: Specification of the HV module

Item	Value
Output Voltage	0 10kV for HV
	0 500V for AD bias voltage
Supply voltage	10 V
Current	$\sim$ 120mA
Control voltage	0 $\sim$ 4 V
Enable voltage	5 V (on) / 0 V (off)

2.7 Goal of this thesis

The most desirable solution to Hyper-K photosensor is to develop the high QE version of 50 cm HPD which satisfy the requirements to photosensors in Hyper-K because it is

TABLE 2.3: Specification of the preamplifier

Item	Value
Band width	25 MHz
Gain	∼50 kV / A
Supply voltage	5 V
Current	∼15 mA
Output impedance	50 Ω

TABLE 2.4: Specification of the control power supply

Item	Value
Output voltage	10V for HV module
	0∼4 V for HV and AD bias control voltage
Supply voltage	100V AC

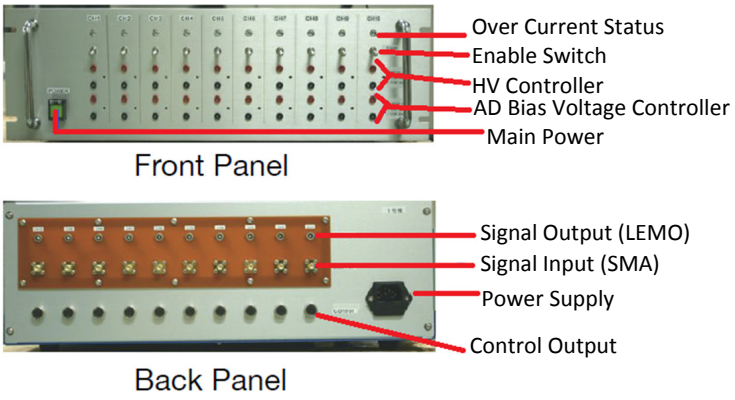

FIGURE 2.12: The control power supply

expected to have better performance than the other options. However, this is the first time in the world that the large-aperture (50 cm) HPD is developed for water Cherenkov detector. There would be many difficulties involved.

As a result, we developed the prototype of 20cm HPD with QE 20% as a first step and evaluated its performance [1]. However, the HPD has a certain temperature dependence because of the AD as stated in Section 2.5.1. In order to understand the performance of the HPD under the Hyper-K operational environment more exactly, we measured the temperature dependence of the HPD. The method and result of the temperature dependency measurement is described in Section 3.1.

Based on the development experience of the 20cm HPD, we developed a prototype of 50 cm HPD with ϕ5 mm AD, which has the same diameter as the one used in 20cm HPD and evaluated its performance. The signal response of single p.e. has been evaluated before [2]. In this thesis, the detailed performance, including transit time spread, linearity,

dark count rate and temperature dependency of gain will be measured and described in detail in Section 3.2. It should be noted that the collection of the HPD with ϕ5mm AD is only about $\sim$ 8% so it is cannot be used in the Hyper-Kamiokande. The purpose of its production and evaluation is just to test the High QE technology and the large diameter HPD production technology.

In order to ensure the collection efficiency, a large area AD (e.g. ϕ20 mm) is proposed to be utilized in 50 cm HPD. However, the increase of the AD area will lead to a larger junction capacitance therefore the noise level will be high. Several solutions have been proposed to resolve this issue. In this thesis, two solutions: the development of a new kind of preamplifier with decoupling transformer and the development of a multi-channel AD will be discussed in detail. The performance of the 50 cm HPD with 5ch 20mm AD and 50 cm HPD with 14.7 mm AD and decoupling transformer will be described in detail in Section 4.1 and Section 4.2.

Furthermore, the development status of HV supply, including HV module selection, external HV supply and measurement of on-off resistant, is described in Chapter 5.

To sum up, it will be shown in this thesis that the HPD has a great potential as a Hyper-Kamiokande photo-detector. The development of HPD is ongoing.

Chapter 3

Performance evaluation of HPD with ϕ5 mm AD

The performance of HPD with ϕ5 mm AD, including 20cm version and 50 cm version with the pre-amplifier is described in this chapter.

3.1 The Temperature dependency of 20cm HPD with ϕ5 mm AD

The performance of 20cm HPD with ϕ5 mm AD has been evaluated fully. It is confirmed that the 20cm HPD with ϕ5 mm AD has better performance than that of Super-K PMT [1]. However, the HPD has a certain temperature dependence because of the AD (Section 2.5.1). The operating ambient temperature at Hyper-K will be approximately 13 °C, while the environment temperature outside of Hyper-K during production, preparation or development is higher. Nevertheless, the temperature might fluctuate during operation because of heat from electronics in the HPD or other reasons. In order to understand the performance of the HPD under the Hyper-K operational environment more exactly, we measured the temperature dependence of the HPD.

Moreover, we also measured the temperature dependence of the AD's performance alone to determine its contribution to that of the HPD. The temperature dependence of the

preamplifier has been measured before: the temperature coefficient of the gain (noise) is -0.032 %/°C (-0.0026 %/°C).

3.1.1 Method

In order to measure the temperature dependence of the AD or the HPD, we need to measure their performance like gain in different temperature, while other conditions like the number of incident photons or the bias voltage of the AD are constant. Therefore, we divided the setup for the temperature dependence measurement into two parts: the light source part, which consists of an LED (λ = 430 nm, pulse width = 200 ns), as the light source and a PMT for monitoring luminosity, and the measurement part, which consists of the sample and a preamplifier. Not only the measurement part was put into a thermostatic chamber to get its temperature controlled, the light source part was also put into another thermostatic chamber to stablilize its temperature so as to avoid the instability of the light intensity. The temperature in each thermostatic chamber was measured by a thermometer put near by the photosensor. Between these two thermostatic chambers, an optical fiber was used to transmit the light generated by the LED to the photosensors, which would be measured (Fig. 3.1).

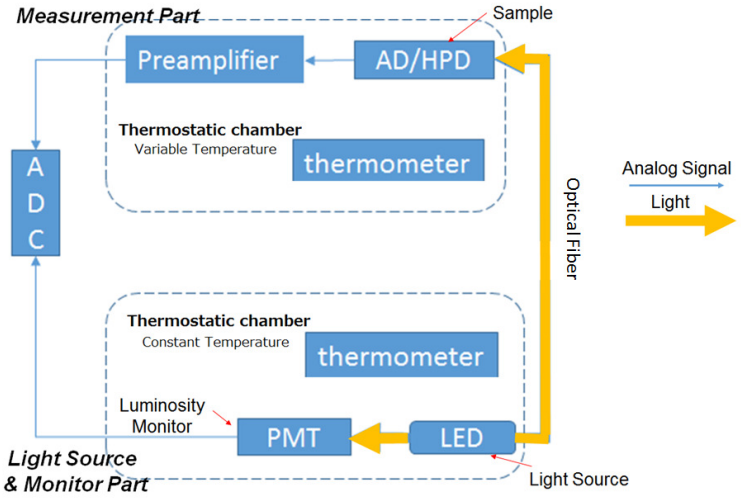

FIGURE 3.1: Setup to measure temperature dependency

3.1.2 The temperature dependence of gain

The typical charge distribution of an 20cm HPD with the applied HV of 7.6 kV and the AD bias voltage of 339 V at 15 °C is shown in Fig. 3.2. The HPD has an excellent single

photoelectron (p.e.) distinguishability comparing with conventional PMTs: the single p.e. peak can be seen more clearly.

The HPD's gain is calculated according to the charge of the single p.e. signal. By monitoring the single p.e. signal charge by changing the temperature, we measured the temperature dependence of the HPD's gain. As shown in Fig. 3.3, the black points represent the gain of the HPD, while the red points represent the temperature in the thermostatic chamber in which the HPD was put. The time series variation of the gain data after the temperature changed is exponential and the stabilized value is obtained by fitting.

The AD's gain under different temperature is calculated from the relative change of the AD's output under different temperature to the output at a base temperature (20 °C in this case), at which gain is known from the AD's product specification. This method is also used to make a cross check when we measured the temperature dependence of gain of the HPD.

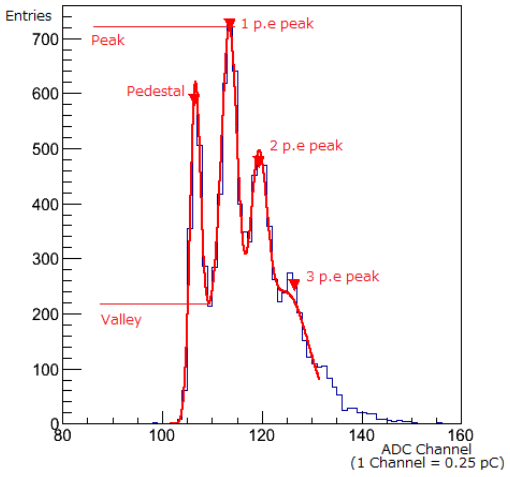

FIGURE 3.2: The signal distribution of an 20cm HPD

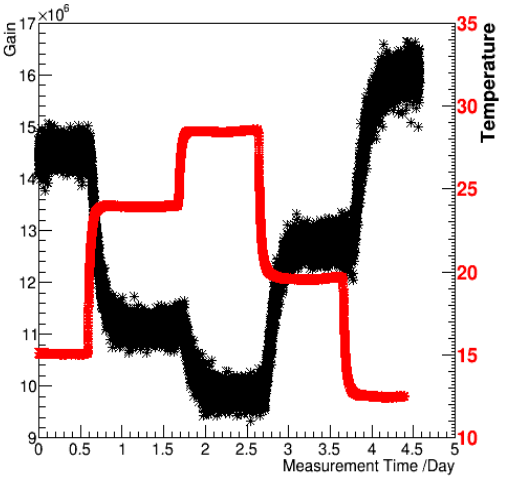

FIGURE 3.3: An example of the temperature dependence measurement of the HPD

TABLE 3.1: The temperature dependence of the gain of the AD and that of the HPD (with preamplifier) at AD bias voltage of 300 V, 20 °C

Sample	Gain	Temperature Coefficient of Gain
AD	124	-2.4%/ °C
HPD*	1.22×10^7(250*)	-2.4%/ °C

*: The gain of the AD which is equipped in the HPD. This value is obtained from the HPD's product specification.
**: HV of HPD is 8kV.

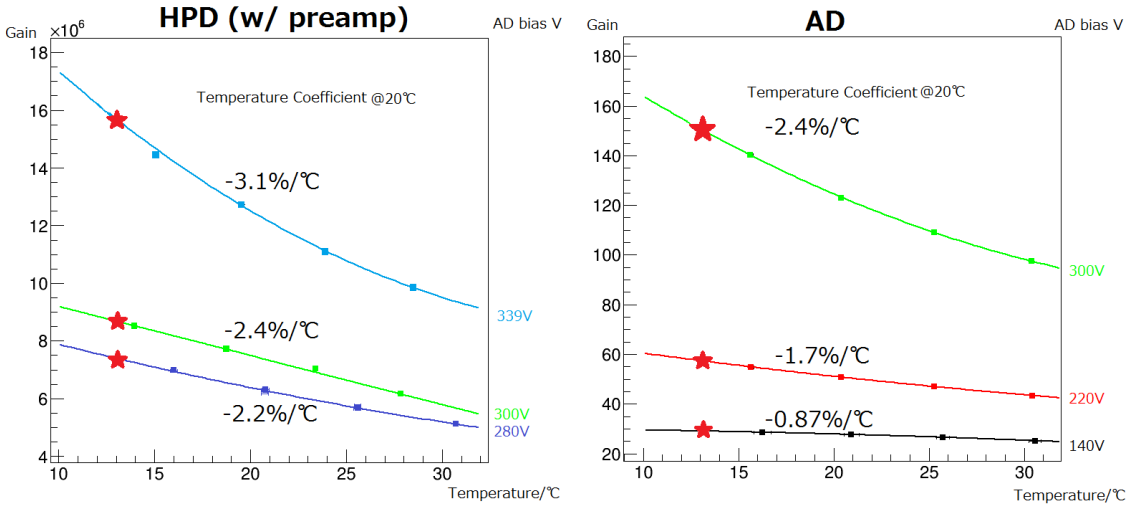

FIGURE 3.4: The temperature dependence of the gain of the HPD with preamplifier (left) and that of the AD (right)
*: The red star represents the expected value at the temperature of Hyper-K (13 °C)

The relationship between the temperature and the gain is fitted by a quadratic function (Fig. 3.4). By comparing the gain curve under different AD bias voltage, it is easy to find that the AD with higher voltage applied has a more clear temperature dependence. The temperature dependence of the gain of the HPD is primarily due to the AD because the temperature coefficient of the AD and the HPD at the same AD bias voltage (300 V) are matching. (Table 3.1).

3.1.3 The temperature dependence of single photoelectron charge resolution

The single photoelectron charge resolution is defined as the ratio of the root mean square (RMS) to the mean of the single p.e. peak in the charge distribution (Fig. 3.2). A sufficient single p.e. charge resolution is important to detect low energy events. The width of the single p.e. peak is related to the statistical fluctuation of gain, including bombardment gain and avalanche gain, and the noise from the AD or other electronic components. The temperature dependence of the single p.e. charge resolution of the HPD, when the AD bias voltage is 339 V, is shown in the left figure of Fig. 3.5. The single p.e. charge resolution of the HPD (30.0%) is better than that SK PMT (∼60% [1]) under operational temperature 13 °C.

The contribution from the AD's noise to the single p.e. charge resolution is also calculated. Here, the AD's noise is defined as the RMS of the AD's pedestal charge distribution and the expected single p.e. signal level of the HPD is calculated by the multiplication of the electron's charge, the bombardment gain, the avalanche gain and the gain from preamplifier. The contribution is defined as ratio between the AD's noise and the expected single p.e. signal level of the HPD. Its temperature dependence is shown in the right figure of Fig. 3.5.

Apparently, the single p.e. resolution becomes worse with a higher temperature for both the AD and the HPD. This result is as our expected because with the increase of temperature, the gain of AD decreases and the noise, mainly from the preamplifier, increases.

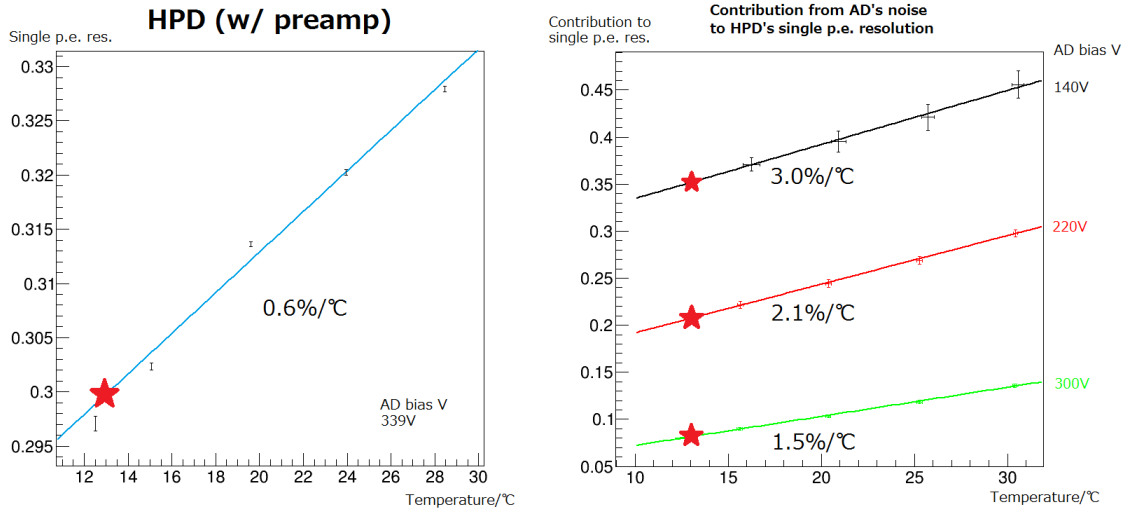

FIGURE 3.5: The temperature dependence of the single p.e. charge resolution of HPD (left) and the contribution from AD's noise (right)
*:The red star represents the expected value at the temperature of Hyper-K (13 °C).
**:The temperature coefficient is a relative value.

3.1.4 The temperature dependence of peak/valley of the HPD

The single p.e. distinguishability is evaluated by the value of peak/valley (p/v), where the peak means the height of single photoelectron peak and valley means the value of the valley between the pedestal peak and the single p.e. peak (Fig. 3.2). A higher p/v value also implies a better distinguishability of the single p.e., thus the ability to observe the low energy event is better.

Obviously, the p/v value is better in lower temperature (Fig. 3.6) because of higher gain (Fig. 3.4) and lower noise (Fig. 3.5). And the p/v value of the HPD (4.4) is higher than that of SK PMT (1.9 [1]) under operational temperature, 13 °C.

3.1.5 The temperature dependence of dark count rate of the HPD

The dark count rate, which is the average rate of hit without any incident light, is another important parameter to decide the ability to detect the single p.e. Any pulse higher than a given threshold (half of the single p.e. pulse height, 0.5 p.e., in the case of the HPD) would be treated as a signal and be recorded. Therefore, the singal acquisition could be more effective when the dark count rate as an important non-physics background, is reduced. The dark events are mostly of thermal origin and can therefore be strongly suppressed by cooling the detector (Fig. 3.7). The black line is the result of the gain of 1.25×10^7 while the red line is for the gain of 1×10^7. The blue point represents the dark count rate of the SK PMT at 13 °C, 4 kHz when the threshold is 0.25 p.e. It should be noticed that the dark count rate of the SK PMT cannot to be compared with the dark count rate of the HPD here directly because the diameter of their photocathode is different: 50 cm for SK PMT while 20cm for HPD. The dark count rate of 50 cm HPD measurement will be described later (Section 3.2.4 and Tab. 4.4 in Section 4.2.3).

3.2 Performance Evaluation of 50 cm HPD with ϕ5mm AD

After success fabrication of 20cm HPD, we made the 50 cm HPD with $\phi 5mm$ AD, which has a larger photocathode but a same size AD, evaluated its performance. Although our target design is an HPD with ϕ20mm AD, the only difference between the 50 cm HPD with ϕ5mm AD and our target design is the size of the AD. By evaluating the 50 cm HPD with ϕ5mm AD, we can test the High QE technology and the large diameter HPD production technology. After the production of the 50 cm HPD with ϕ5mm AD, the QE of the photocathode has been evaluated by Hamamatsu and it is found that the QE is as high as expected.

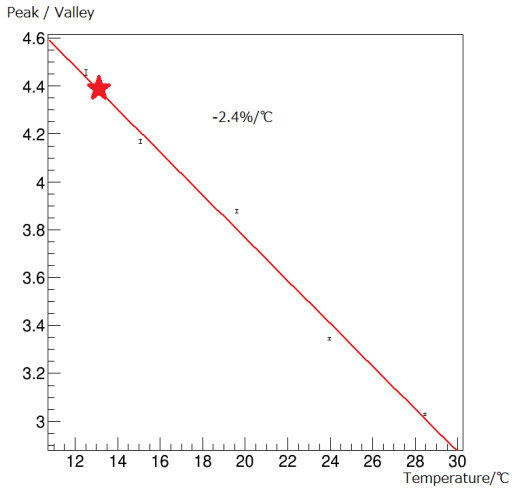

FIGURE 3.6: The temperature dependence of peak/valley of the HPD

*:The red star represents the expected result of the HPD at the temperature of Hyper-K.

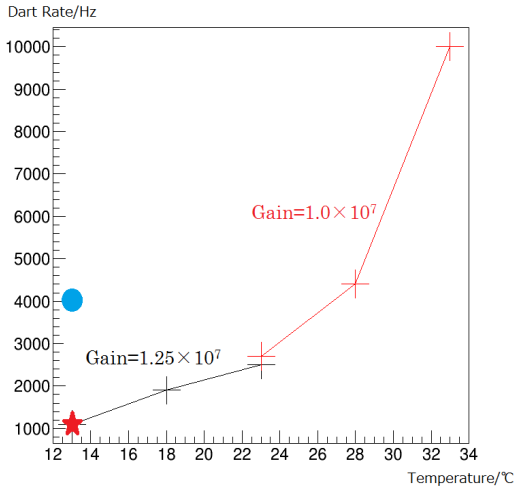

FIGURE 3.7: The temperature dependence of dark count rate of the HPD

*:The red star (blue circle) represents the expected result (real value) of the HPD (SK PMT) with threshold of 0.5 p.e. (0.25 p.e.) at the temperature of Hyper-K

3.2.1 Signal response of single p.e.

The signal response of single p.e. of 50 cm HPD with ϕ5mm AD has evaluated and summarized in Tab 3.2 [2].

Similarly to the performance of 20cm HPD with 5mm AD, the single p.e. resolution and p/v value of 50 cm HPD with 5mm AD is better than that of SK PMT, while the pulse shape is slower slightly. The reason of a slower response is due to the preamplifier. In fact, the HPD itself has very fast response, the rise time of 1.7ns and the fall time of 2.7ns, without amplifier. New preamplifier is being developed to obtain better performance.

TABLE 3.2: Signal response of 50 cm HPD with 5mm AD

	HPD with 5mm AD	Super-K PMT [2]
Rise Time (ns)	7.4	10.6
Fall Time (ns)	11.5	13.1
Pulse width (FWHM) (ns)	25.5	18.5
1p.e. resolution (σ/μ)	16%	53%
Peak / Valley ratio	3.9	2.2

3.2.2 Transit time spread

As has been stated in Section 2.1.3, a good time resolution is important for the event reconstruction. Generally, the time resolution of a photo-sensor is evaluated by the transit time spread (TTS), which is temporal fluctuation from photon emission (t_1) to signal appearance (t_2). For HPD, the drift path of the electron in vacuum tube is almost constant, which is confirmed by simulation and the result of a 20cm HPD without preamplifier, the TTS is dominated by the preamplifier.

The setup for this study is as Fig. 3.8. A TDC was used to measured the time of the synchronization output of laser diode as t_1 and the output time of a discriminator as t_2. The threshold of discriminator is set to 0.5 p.e. For the laser diode we used, the spread of time difference between the synchronization signal output and the light signal output is less than 10 ps, which is confirmed by using an APD. Therefore, it will not influence our experimental precision to regard the time of the synchronization output of laser diode as the time of the light signal output.

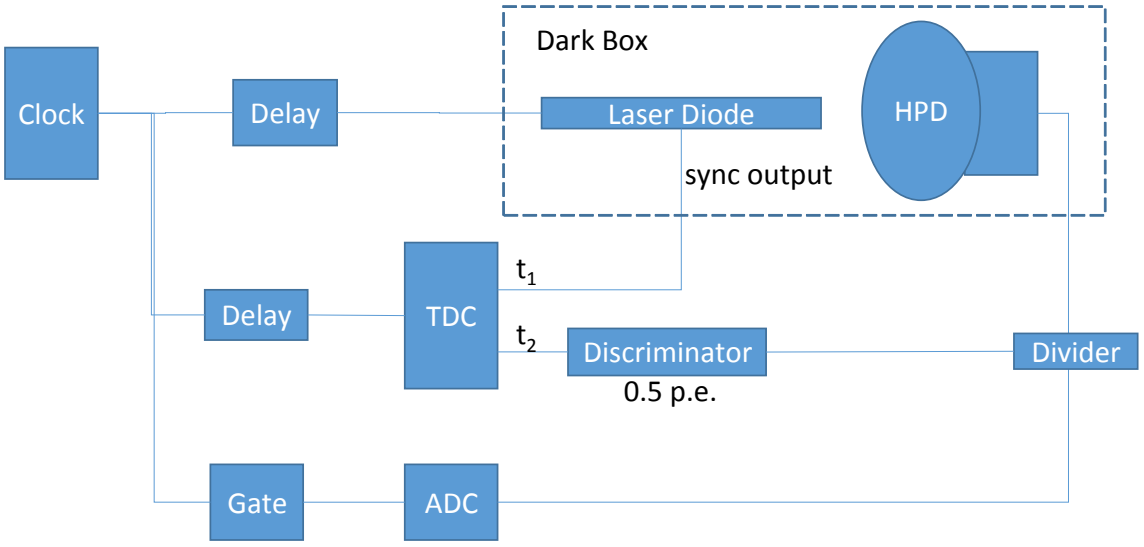

FIGURE 3.8: Setup for the transit time spread measurement

Fig 3.9 shows the relationship between the charge output of HPD and the time of signal appearance ($t_2 - t_1$). The time walk effect can be seen clearly. In order to remove this effect, this figure was fitted by a sum of a inverse proportion function and a linear function and the time spread was calculated after this correction.

Fig 3.10 shows the relationship between the luminosity and the TTS of HPD. We can see that with the number of incident photoelectron increasing, the transit time spread

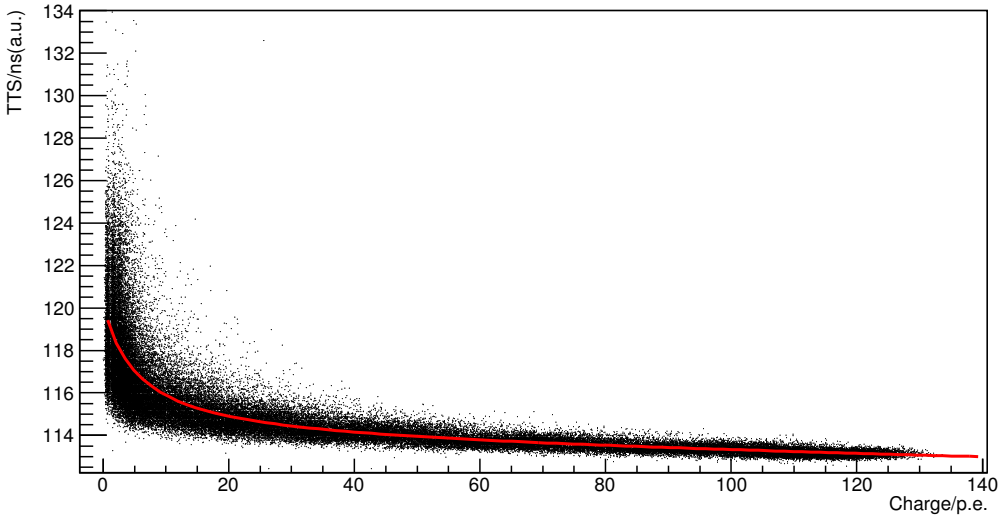

FIGURE 3.9: The relationship between the charge output of HPD and the time of signal appearance

becomes smaller, which means that the time resolution becomes better. For single p.e. level, the TTS is 1.15ns. It is a little bit worse than that of 20cm HPD (0.86ns [1]) due to longer drift path of photoelectron in vacuum tube but better than that of SK PMT (2.2ns [31]).

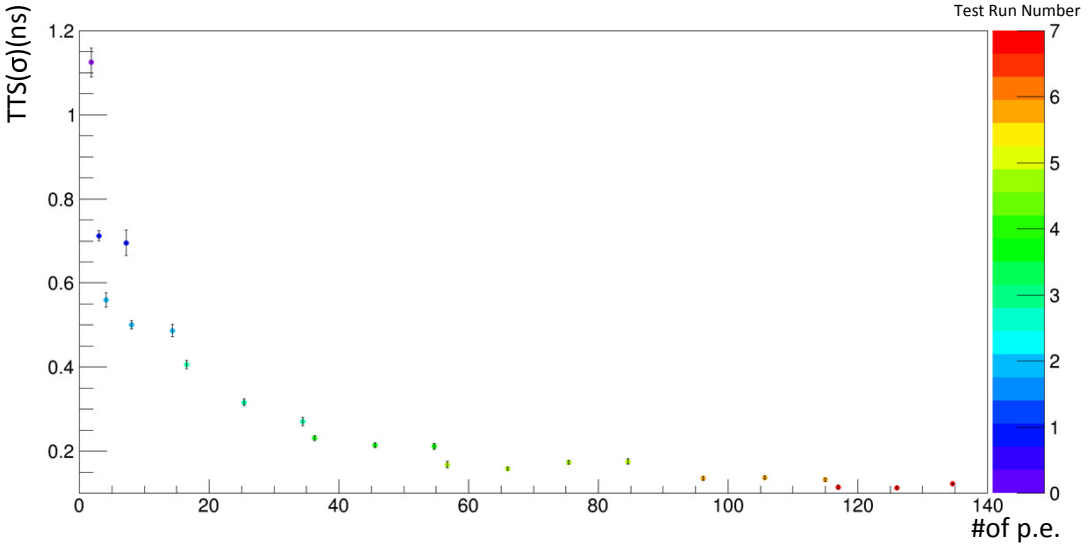

FIGURE 3.10: The relationship between the luminosity and the TTS of HPD
The color of every point represents different test run number.
Luminosity in each test run is different.

3.2.3 Linearity

The linearity of a photo-sensor is the characteristic that the output of the photo-sensor is proportional to the luminosity of incident light. Comparing with the photon multiplier tube, the linearity and dynamic range of the HPD is expected to be better because the avalanche multiplication, which happened in the the AD, is harder to saturated than the dynode used by the PMT. As a result, the linearity of the HPD is mainly limited by the output limitation of preamplifier.

3.2.3.1 Linearity measurement in low luminosity

The linearity of HPD in low luminosity (∼several p.e.) is measured by the peak position in the multi p.e charge distribution. The relationship between the output and the number of photon electron is showed in Fig 3.11. The maximum deviation from the linear line is about 2%.

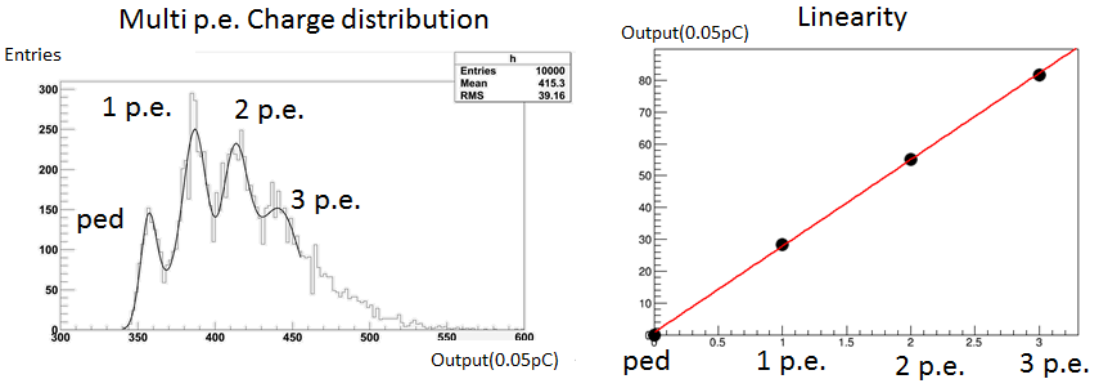

FIGURE 3.11: Gain Linearity in low luminosity
Measurement Condition: HV: 8kV, LV: 293V

3.2.3.2 Linearity measurement in high luminosity and dynamic range

For the linearity in high luminosity, we did the unbiased measurement using two light sources, Laser Diode A and Laser Diode B (Fig. 3.12). When light source A (B) is lighting, the number of incident photons is A (B), and we can measure the output charge of HPD is $O(A)$ ($O(B)$). Now, if we lighted the source A and B simultaneously, the number of incident photons would become to A + B, and the output charge is $O(A+B)$. Obviously, the expected value of $O(A+B)$ equals to the sum of the output

charge when light source A and B lights only $O(A)+O(B)$ (Fig. 3.13). By changing the luminosity of the light source from the region where the linearity has been confirmed to higher region recursively, the linearity in wide range can be evaluated. This method can measure the linearity without bias because there is no other photo-sensor for reference.

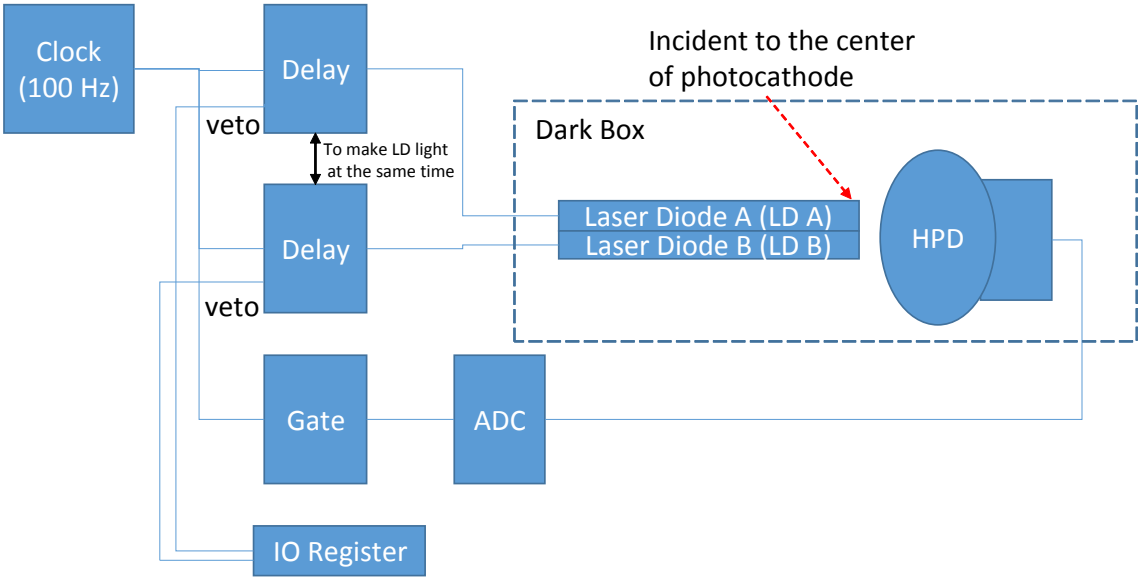

FIGURE 3.12: Setup for the gain linearity measurement in high luminosity

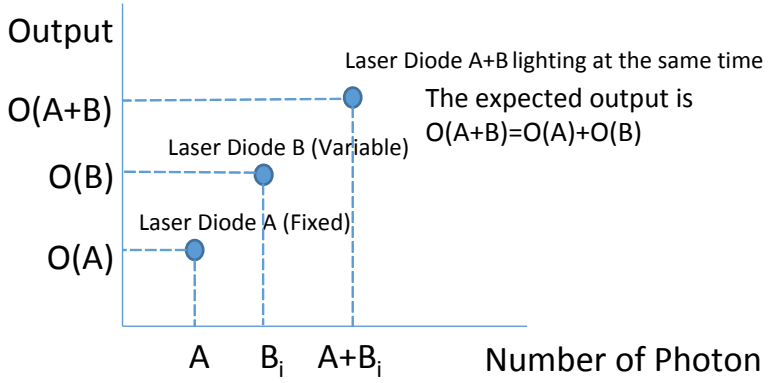

FIGURE 3.13: Principle of the gain linearity measurement in high luminosity

Fig. 3.14 shows the output charge as a function of the number of the input photoelectrons. It is confirmed that the linearity holds up to around 140 photoelectrons, with the maximum drift of 6% (Fig. 3.15). This is worse than Super-K PMT, whose output is linear up to 200 photoelectrons [31]. The dynamic range of HPD will be improved in a next version of the preamplifier because it is limited mainly by the maximum output voltage (~800 mV in current version) of the preamplifier. The reason of the shape in right figure is still investigation. It might come from the nonlinearity of the preamplifier.

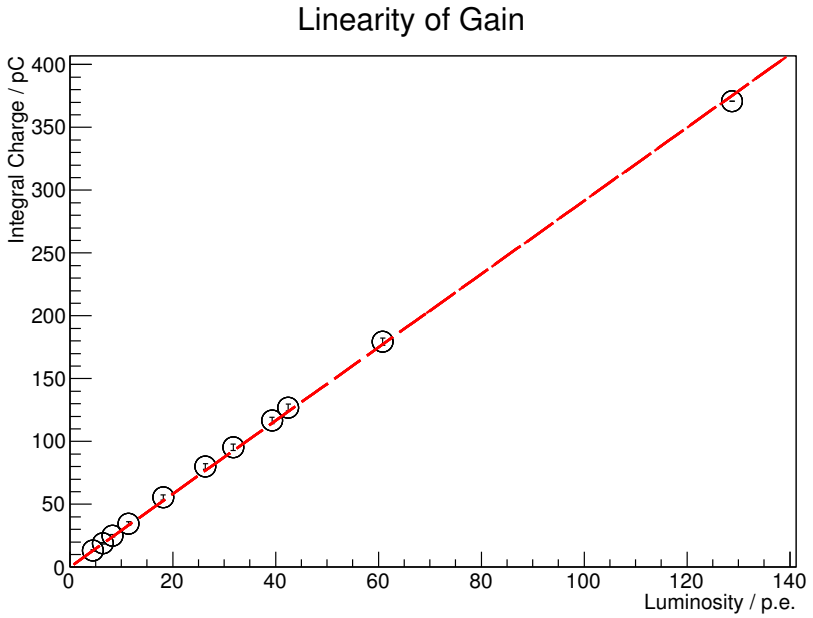

FIGURE 3.14: Relationship between output charge and luminosity
Measurement Condition: HV: 8kV, LV: 293V

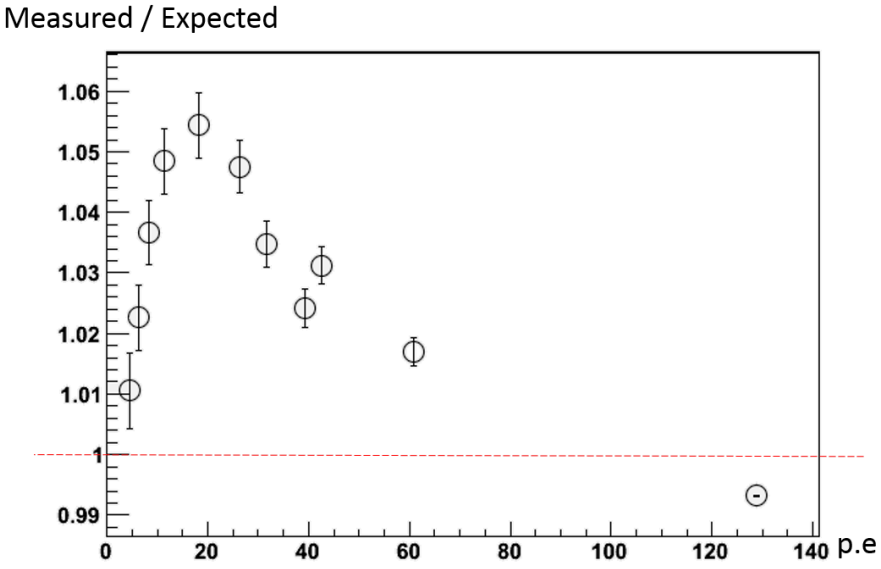

FIGURE 3.15: The change of the deviation from the linear assumption with luminosity
Measurement Condition: HV: 8kV, LV: 293V

3.2.4 Dark count rate

The dark count rate is measured as a function of the threshold. In this measurement, an Analog Timing Module (ATM) board, which was used in Super-K I, II and III as a DAQ board, is used as a discriminator to apply a threshold to the signal of HPD. A

detailed description for ATM can be found in Ref. [32]. The threshold of ATM can be set from 0 mV to 12.5 mV by remode.

Figure 3.16 shows the measured dark count rate of 50 cm HPD with 5mm AD, at room temperature ($\sim$ 24°C). The dark count rate is 0.8kHz at 0.5 photoelectron. After considering the low collection efficiency (CE) of the HPD [1] due to the ϕ5 mm AD ($\sim$ 8%), the dark count rate is about 9.3 kHz for an HPD with a ϕ20 mm AD (93.3%).

When used in a water Cherenkov detector, the dark count rate of 50 cm HPD is expected to decrease with operation time in the dark environment and with lower temperature (13°C) in the water tank. According to the temperature dependency of dark count rate of 20cm HPD (Section 3.1.5), the dark rate of 50 cm HPD with 20mm AD can be reduced to 1/2 (i.e. 4.7 kHz), which is the same level as the Super-K PMT.

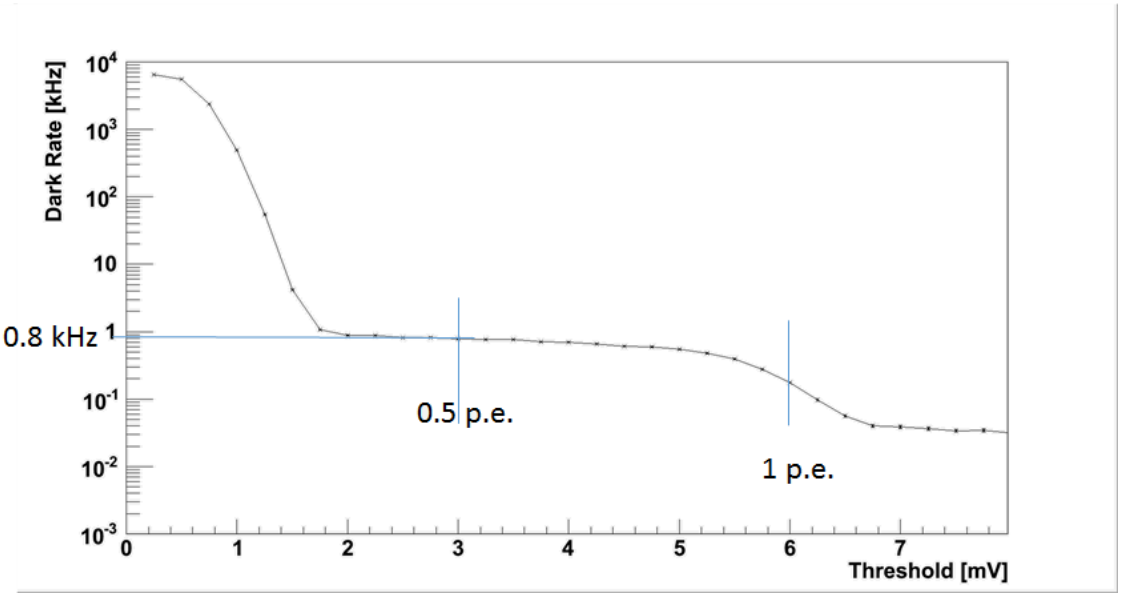

FIGURE 3.16: The relationship between dark count rate of HPD and threshold
Measurement Condition: HV: 8kV, LV: 293V

3.2.5 Temperature dependency of gain

Similarly, the temperature dependency of gain of 50 cm HPD with ϕ5mm AD has been evaluated (Fig. 3.17). Due to the time constraint, only one AD bias voltage (253V) has been tested.

[1] Collection efficiency of HPD is measured by counting the hit number when HPD is illuminated uniformly and perpendicularly to the surface of cathode.

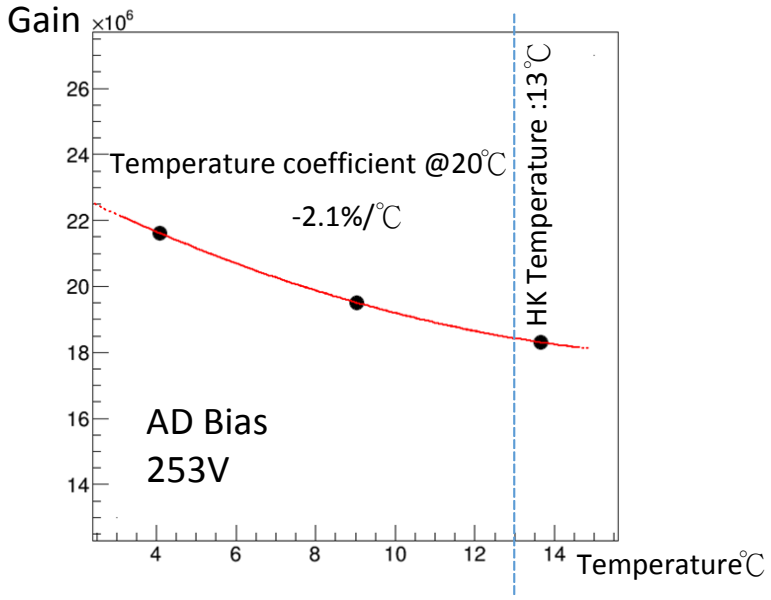

FIGURE 3.17: Temperature dependency of gain of 50 cm HPD with 5mm AD
Measurement Condition: HV: 8kV, LV: 253V

Comparing with the result of 20cm HPD and that of 5mm AD (Fig. 3.4), it is easy to find that their temperature coefficient have similar values, because the diameter of the AD is 5mm for all of them. Furthermore, the temperature dependency of HPD is stronger for higher AD bias voltage. Even though, when AD bias voltage is 339V, the temperature coefficient is only about $\sim -3.1\%/°\mathrm{C}$. In Hyper-K, surrounding water temperature is expected stable (variation $\sim 0.01°\mathrm{C}$). The temperature dependence of AD will not influence the stability of HPD in Hyper-K.

3.3 Summary of the performance evaluation of HPD with ϕ5 mm AD

The performance of the HPD with ϕ5 mm AD, including 20cm HPD and 50 cm HPD has been evaluated in the room temperature ($\sim 20°\mathrm{C}$). Both of them have better performance expect dynamic range (and the collection efficiency for 50 cm HPD with ϕ5mm AD) than that of SK PMT and satisfy the requirements to Hyper-K photosensor (Tab. 3.3). As for the temperature dependency, in fact, the performance of HPD is better, (i.e. lower dark rate, higher 1 p.e. resolution and higher peak / valley ratio) when it is in the Hyper-K environment ($\sim 13°\mathrm{C}$) than when it is in the room temperature.

Moreover, the temperature dependence is so small (2%/°C) that the performance and the stability of the HPD will not be influenced when the HPD operates in the Hyper-K experiment.

TABLE 3.3: Performance of HPD with ϕ5 mm AD

	20 cm HPD w/ 5 mm AD[1]	50 cm HPD w/ 5 mm AD	SK PMT	Hyper-K Requirement
Rise Time (ns)	∼10	7.4[2]	10.6	10
Time resolution σ@ 1 p.e. (ns)	0.86	1.15	2.2	2.2
1p.e. resolution (σ/μ)	12%	16%[2]	53%	50%
Peak / Valley ratio	5.6	3.9[2]	2.2	1.9
Dynamic range (p.e.)	60	140	200	1000
Dark count rate	2 kHz	0.8 kHz	4.2 kHz	Not decided

At nominal gain: 10^7

However, the gain linearity of the HPD with current preamplifier, is only kept until 140 p.e., lower than the requirements (1000p.e.) As has been stated in Section 3.2.3, the dynamic range of HPD is limited by the specification of the preamplifier. We will improve the preamplifier to satisfy the requirements in the future version of the HPD.

In addition, the good performance of the 50 cm HPD with 5mm AD also gave us confidence to produce our target design: 50 cm HPD with 20mm AD. It is shown that there are no problem on the High QE technology and the large diameter HPD production technology. In next Chapter, the detail introduction to the development of 50 cm HPD with 20mm AD is described

Chapter 4

R&D of 50 cm HPD with a large area AD

In order to ensure a high collection efficiency (CE), a larger area AD is desired for 50 cm HPD. According to the simulation result from Hamamatsu, a ϕ20 mm AD can make the CE reach to $\sim$ 93% while the collection efficiency of a ϕ5 mm AD is less than $\sim$ 10%. So the 50 cm HPD with ϕ20 mm AD is our target design. However, with the increasing area of AD, the parasitic capacitance also becomes larger, which leads to a higher noise level [4]. The capacity of a $5mm\phi$ AD is only 60pF while the capacity can reach 800pF for a ϕ20 mm AD.

Furthermore, the large junction capacitance will also lead a longer time constant of the readout circuit, which means that the width of the signal pulse will increase. At the same gain of HPD, or the same integrated output charge, a wider signal means a lower pulse height, which will enhance the difficulty of trigger further. On the other hand, a wider pulse, in other words, a longer rise time, will also reduce the timing resolution: the pulse shape is more easily to be influenced by the noise and the baseline shift.

Several countermeasures are proposed to reduce the noise level as following.

- Application of segmented AD, or multichannel AD
- Preamplifier Improvement
  - Application of decoupling transformer

  - Boot strap circuit
  - Non-feedback amplifier

- New AD with low capacitance

Here, the application of segmented AD and the decoupling transformer will be described in detail.

The segmented AD will be introduced in Section 4.1. 2 kinds of AD with 20mm ϕ, 2ch AD and 5ch AD has been produced, installed to the 50 cm HPD and tested. The 50 cm HPD with 5ch ϕ20 mm AD shows a good single p.e resolution while the one with 2ch ϕ20 mm cannot distinguish single p.e. The junction capacitance of 400 pF, for one channel of the 2ch ϕ20 mm AD is still too large for current preamplifier. As a result, in section 4.1, we will introduce the performance of the 50 cm HPD with 5ch ϕ20 mm AD only.

The decoupling transformer will be introduced in Section 4.2 in detail, including the principle, the performance test result of the decoupling transformer on a single ϕ20 mm AD and on a 50 cm HPD with ϕ14.7 mm AD, another prototype of 50 cm HPD. The 50 cm HPD with ϕ14.7 mm AD also has a collection efficiency of $\sim$ 80%. The junction capacitance of the ϕ14.7 mm AD is $\sim$ 450 pF. The reason of testing the effort of the decoupling transformer on this HPD rather than the HPD with ϕ20 mm AD is just due to the time constraint. It will be tested on the 50 cm HPD with ϕ20 mm AD in the future. Except the signal response, the dark count rate and the transit time spread of the 50 cm HPD with ϕ14.7 mm AD and decoupling transformer is also evaluated. Furthermore, as will be introduced in Section 4.2.3, there is still some high frequency noise remained, even after applying the decoupling transformer. A 70 m co-axis signal cable is used as the low pass filter and its effect on noise reduction is evaluated.

Since the development of the 50 cm HPD with ϕ20 mm AD, including the AD itself and the preamplifier, is still ongoing, only some preliminary results is shown here. The full evaluation of 50 cm HPD with ϕ20 mm will be done in the future.

4.1 Application of segmented AD

To reduce the capacitance of AD, the most obvious way is to separate it into several parts (channels). Each part is amplified by an isolated preamplifier and then a sum amplifier will sum all the signal to get the final signal. The HPD system with multi-ch AD is as Fig 4.1.

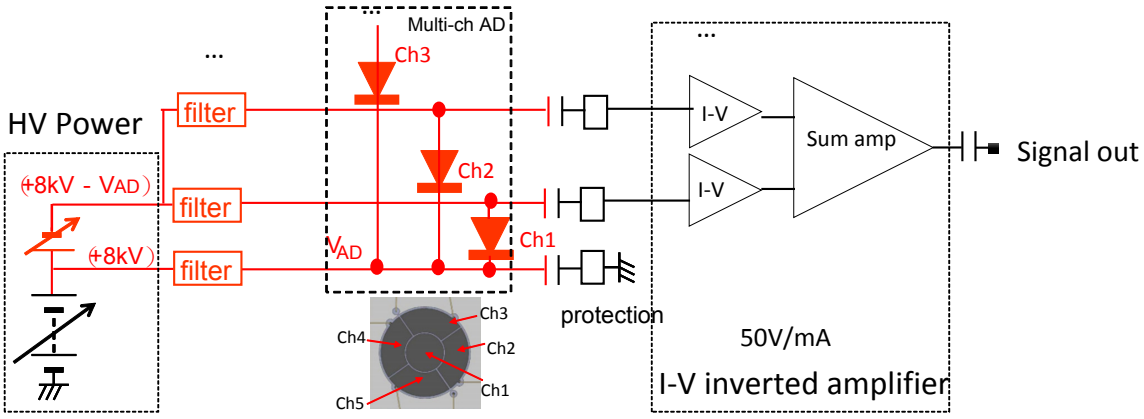

FIGURE 4.1: The HPD system with multi-ch AD
Only 2 connected channels are shown in this figure, although more channels can be connected.

4.1.1 Segmented AD

We developed two kinds of segmented ϕ20 mm AD (Fig 4.2): 2ch AD (left) and 5ch AD (middle and right). Each channel of the AD has the same area. Assuming that the noise level is proportional to the input capacitance of the preamplifier [4], the total noise level of the 5ch AD (2ch AD) is $1/\sqrt{5} \sim 44\%$ ($1/\sqrt{2} \sim 80\%$) of the single channel AD. The total noise level is the square root of the sum of the squares of the noise from each channel rather than the sum of each channel's noise, because each channel is amplified by isolated preamplifier.

4.1.2 Evaluation on 50 cm HPD

The performance of the segmented AD is tested in a 50 cm HPD (THD0031). The output signal is shown in Fig. 4.3. It is shown that the pulse shape of 50 cm HPD with 5ch 20mm AD is slower than that of 50 cm HPD with 5mm AD (Tab. 4.1).

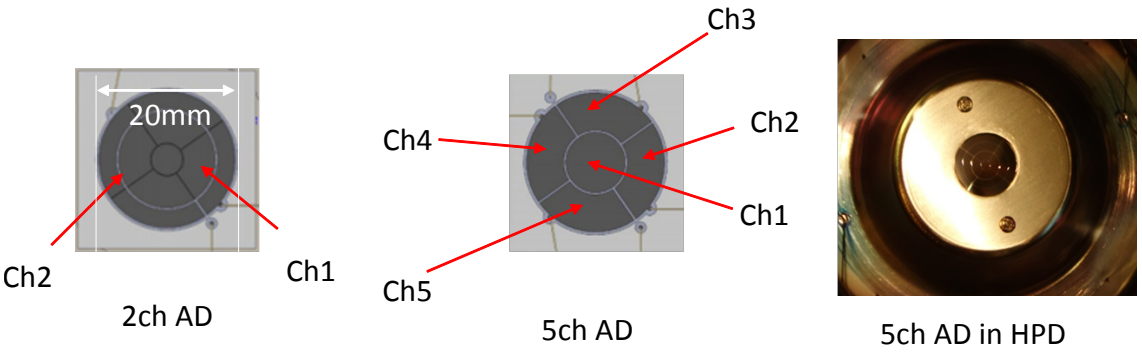

FIGURE 4.2: Multi-channel AD

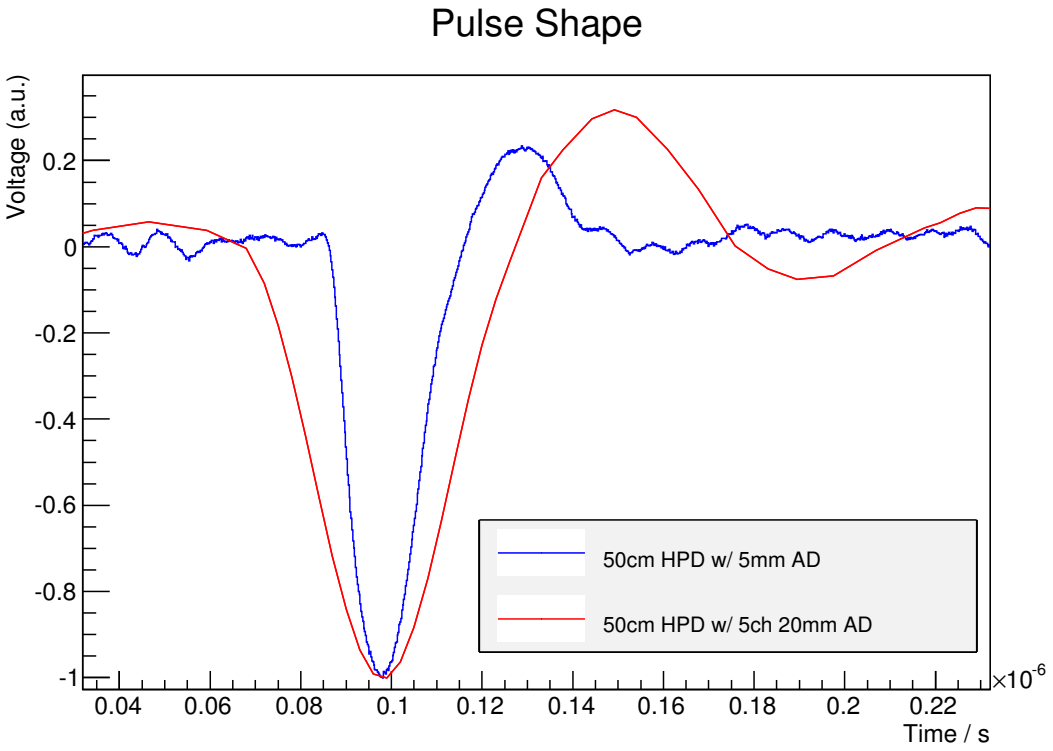

FIGURE 4.3: Pulse shape of 50 cm HPD with 5ch 20mm AD (red) and 50 cm HPD with 5mm AD (blue)
HV: 8 kV LV: 415 V

The charge distribution (Fig. 4.4), we can see that the 50 cm HPD with 5ch ϕ20 mm AD has a better 1 p.e. resolution than the Super-K PMT, although it is lower than that of 50 cm HPD with 5mm AD. (Tab. 4.1, Tab. 3.2).

Both of a slower response and a worse single p.e. resolution is caused by the large AD junction capacitance. Even though the capacitance in each channel becomes 1/5 (160pF), it is still larger than that of 5mm AD (60pF). In addition, more channel for an AD is difficult because of the difficulty of the pin arrangement. The effective area will also decrease due to more isolate trench between each channel.

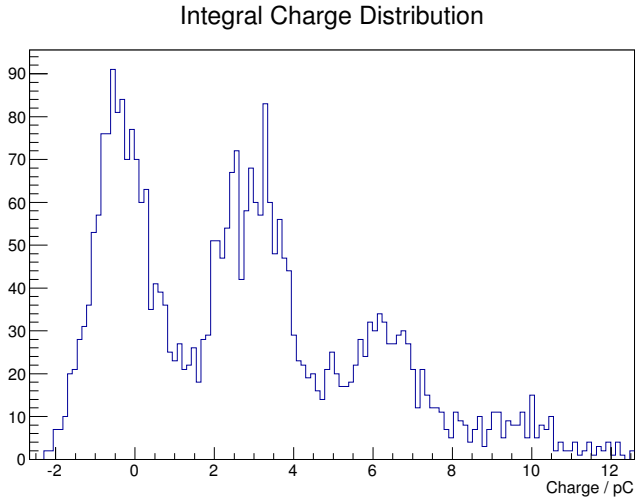

FIGURE 4.4: Integral Charge distribution of 50 cm HPD with 5ch 20mm AD

TABLE 4.1: Single photoelectron characteristics of 50 cm HPD w/ 5ch 20mm AD

	50 cm HPD w/ 5ch 20mm AD	50 cm HPD w/ 5mm AD[2]	SK PMT[2]
Rise time (ns)	20.3	7.4	10.6
Fall time (ns)	21.1	11.5	13.1
Pulse width (FWHM) (ns)	32.3	17.1	18.5
1 p.e. resolution (σ/μ)	28%	16%	53%
Peak / valley ratio	3.1	4.0	2.2

HV: 8.4 kV LV: 415 V

4.2 Application of decoupling transformer

A usual capacitor coupling for deriving a signal from AD at 8 kV brings a large noise due to a large AD stray capacitance. As a result, another coupling transformer is added to reduce the capacitance seen by the amplifier. Therefore the noise generated from the preamplifier can be reduced.

4.2.1 Principle

Let us consider a circuit as Fig. 4.5. The turns ratio of the transformer is $1 : n$. The capacity of C_2 is C_2. The capacity seen from the readout is C_1. I_1 and I_2 represent the current flowing the readout part and the AD part respectively. U_1 and U_2 represent the voltage on the readout part and the AD part (including decoupling capacitor) respectively.

Then,

$$
\begin{aligned}
I_1 &= C_1 \times \frac{\Delta U_1}{\Delta t} \\
I_2 &= C_2 \times \frac{\Delta U_2}{\Delta t} \\
I_1 &= n \times I_2 \\
\Delta U_2 &= n \times \Delta U_1 \\
C_1 &= n^2 \times C_2
\end{aligned}
\tag{4.1}
$$

If n is less than 1, the capacity seen from readout is less than the capacity of the original condenser.

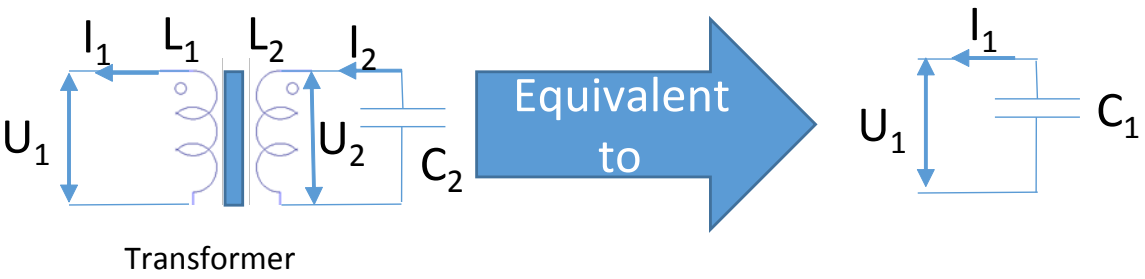

FIGURE 4.5: Principle of the capacitance suppression using decoupling transformer

Then, let's consider the effects of an ideal transformer when it was connected between AD and preamplifier as Fig. 4.6.

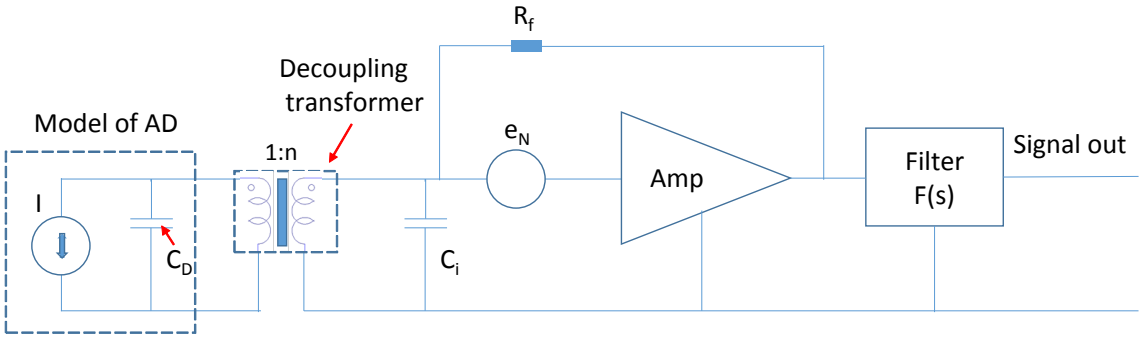

FIGURE 4.6: Ideal transformer coupling between AD and preamplifier[4]

In Fig. 4.6, C_D, C_i and R_f represents the capacitance of detector (the AD in this case), the input capacitance of the preamplifier and the feedback resistance of the preamplifier, respectively. e_N is the noise. $F(s)$ represents the frequency response of the preamplifier. Therefore, the signal-to-noise ratio is given by:

$$\eta_{TRANSF} = \frac{L^{-1}(I(s)F(s)/s)R_f/n}{\frac{R_f}{\sqrt{\left(\frac{1}{\omega(C_D/n^2+C_i)}\right)^2+R_f^2)}}\left[\int_0^\infty e_N(f)|F(j\omega)|^2 df\right]^{1/2}} \tag{4.2}$$

where $I(s)$ is the output current of the AD and L^{-1} is the inverse Laplace transform. This result is similar with the result for a charge sensitive preamplifier given by E. Gatti [4]. Obviously, for a large C_D, the denominator decreases as n^2, while the numerator decreases as n. Therefore, the signal-to-noise ratio would be increased. For a real transformer coupling, more factors, such as the loss due to the transformer and the frequency response of the transformer, should be considered. More details can be found in [4].

4.2.2 Evaluation on a single AD

We tested the performance of the preamplifier with decoupling transformer on a single ϕ20 mm AD in Fig. 4.7. The output luminosity of the light source is set to be same, and the output signals of two types preamplifier, the one with decoupling transformer and the one without decoupling transformer, are shown in Fig. 4.8.

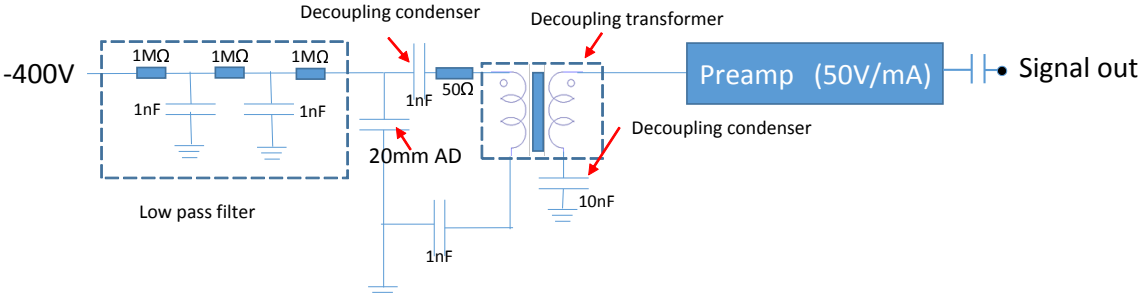

FIGURE 4.7: Circuit for the test of the preamplifier with the decoupling transformer on a single ϕ20 mm AD

Fig. 4.9 and Fig. 4.10 shows the pulse height distribution of pedestal and signal. Pulse height here is defined as the peak value in a certain gate (500ns in this study). As a result, if the noise level is high, the mean of the pulse height distribution of pedestal should be large and the width of the pulse height distribution should be wider because the high level noise comes in to the gate randomly. It is obvious that the noise is reduced to a quarter of the original while the loss of signal is only about 17% (Fig. 4.9, Fig 4.10)

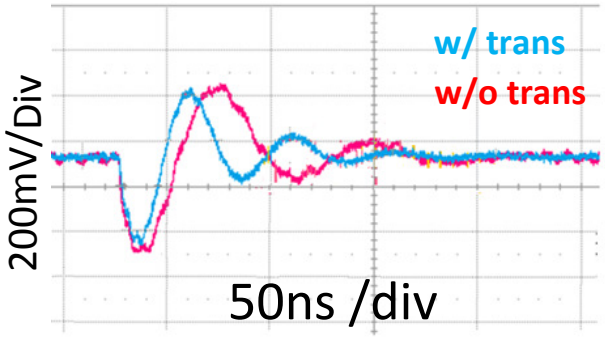

FIGURE 4.8: Pulse shape of a single ϕ20 mm AD output
Blue line represents the pulse shape using the amplifier with decoupling transformer, red line shows the pulse shape using the one without decoupling transformer
AD Bias V: 400V AD: ϕ20 mm AD

due to the insertion loss of transformer. The S/N ratio in the pulse height distribution is increased about 4 times.

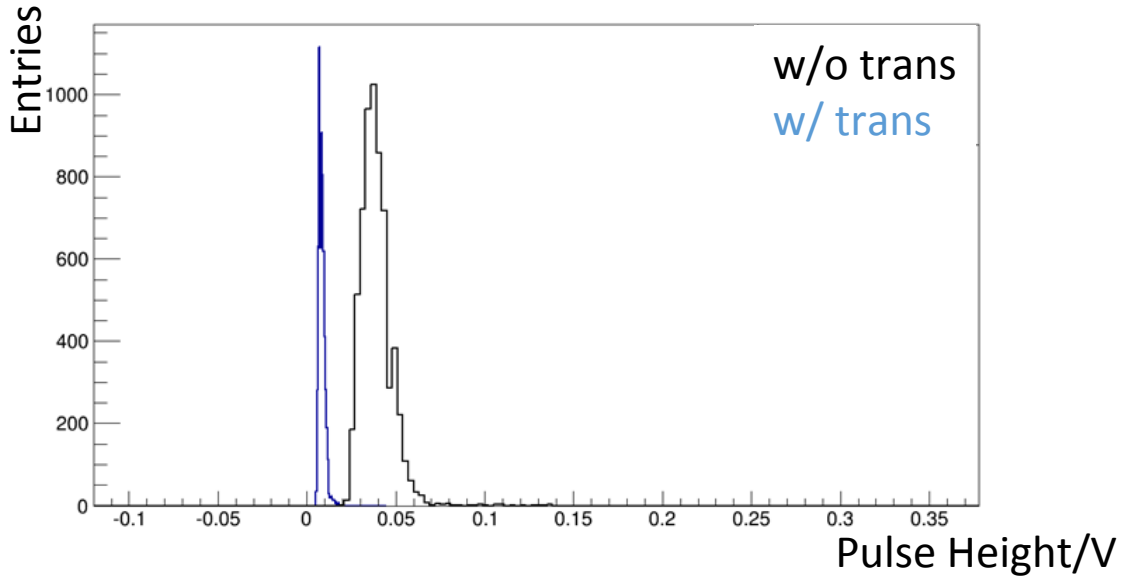

FIGURE 4.9: The pulse height distribution of the pedestal
Blue line represents the pulse shape using the amplifier with decoupling transformer, black line shows the pulse shape using the one without decoupling transformer
AD Bias V: 400V AD: ϕ20 mm AD

For the integrated charge distribution, the noise is reduced to the 73% of the original (Fig. 4.11). Here, the noise is defined as the RMS of the charge output distribution of the pedestal. The integrated charge of signal with gate of 100ns is increased about 1.5 times. Although the pulse height decreased, the integral charge of the signal of the 50 cm HPD with decoupling transformer in high luminosity is 1.59 times of that of

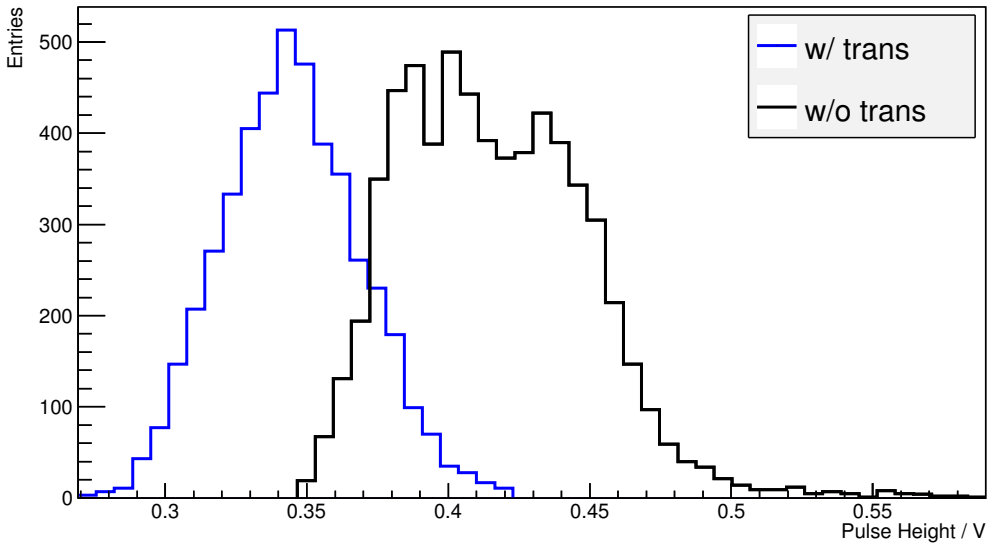

FIGURE 4.10: The pulse height distribution of the signal in high luminosity
Blue line represents the pulse shape using the amplifier with decoupling transformer, black line shows the pulse shape using the one without decoupling transformer
AD Bias V: 400V AD: ϕ20 mm AD

the 50 cm HPD without decoupling transformer (Fig. 4.12) and the S/N ratio in the integrated charge distribution is increased about 2 times. The reason is the contribution from overshoot part is reduced due to a faster overshoot (Fig. 4.8).

4.2.3 Evaluation on 50 cm HPD with a ϕ14.7 mm AD

The performance of the preamplifier with transformer is also tested on a HPD with ϕ14.7 mm AD (THD0041) with circuit shown in Fig. 4.13.

4.2.3.1 Response of multiple photoelectrons

We compared the pulse shape (Fig, 4.14), the integral charge distribution (Fig. 4.15) and the pulse height distribution (Fig. 4.16) of the 50 cm HPD signal with and without the decoupling transformer. In this comparison, the HV is 11kV and the LV is 415V. The gain of HPD with (without) decoupling transformer is 10^7 (1.6×10^7). The reason why the HV is not 8kV is that the single p.e. pulse shape cannot be seen at 8kV for the 50 cm HPD without the decoupling transformer.

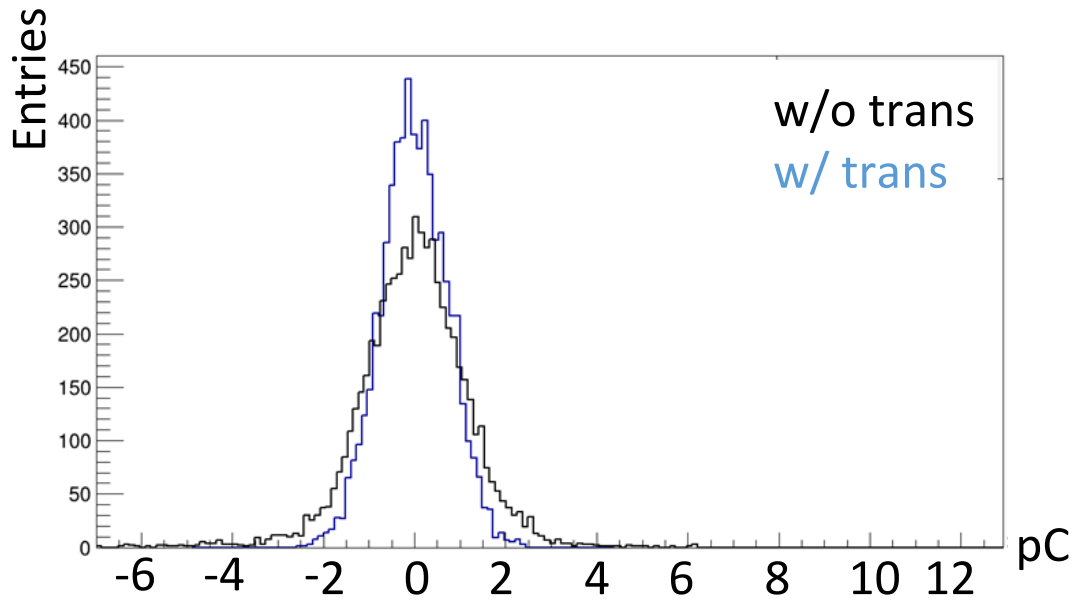

FIGURE 4.11: The integral charge distribution of the pedestal
Blue line represents the pulse shape using the amplifier with decoupling transformer, black line shows the pulse shape using the one without decoupling transformer
AD Bias V: 400V AD: ϕ20 mm AD

Obviously, the decoupling transformer brings a faster response and a better 1p.e. resolution to the 50 cm HPD. The comparison result is shown in Tab. 4.2.

TABLE 4.2: Effect of decoupling transformer on the multi photoelectron response of 50 cm HPD w/ ϕ14.7 mm AD

	50 cm HPD w/ 14.7mm AD and trans	50 cm HPD w/ 14.7mm AD and no trans
Rise Time (ns)	14.3	19.3
Fall Time (ns)	16.7	23.5
Pulse width (FWHM) (ns)	29.5	42.2
1p.e. resolution (σ/μ)	26.9%	49.1%
Peak / Valley ratio	4.9	1.4

For the signal response when HV is 8kV, the pulse shape of single p.e. with ϕ14.7mm AD also can be seen clearly, after applying the 20MHz low pass filter in oscilloscope. The charge of single p.e. in 8kV is shown in Fig. 4.17.

The performance of the 50 cm HPD with ϕ14.7mm AD and decoupling transformer is shown in Tab. 4.3. Even though the decoupling transformer can increase the S/N ratio effectively, the performance of the HPD with decoupling transformer when HV is 8kV is

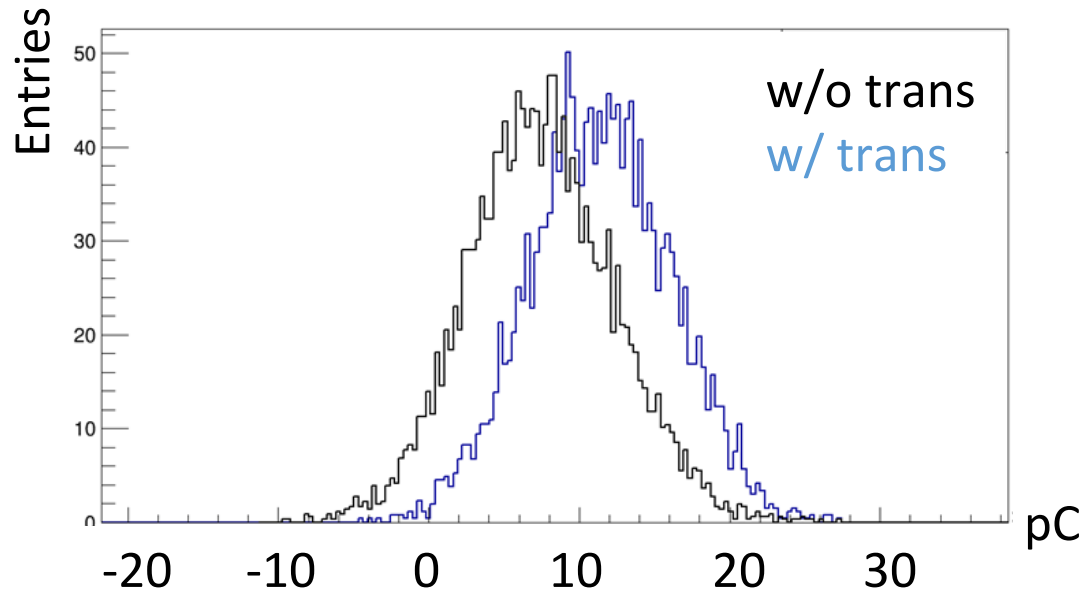

FIGURE 4.12: The integral charge distribution of the signal in high luminosity
Blue line represents the pulse shape using the amplifier with decoupling transformer, black line shows the pulse shape using the one without decoupling transformer
AD Bias V: 400V AD: ϕ20 mm AD

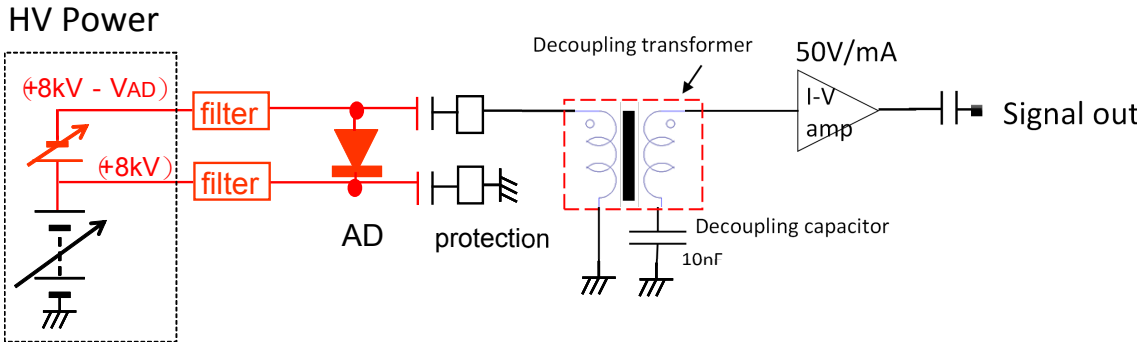

FIGURE 4.13: Circuit of the 50 cm HPD using decoupling transformer

not satisfactory. As a result, we are considering the combination use of the multi-channel AD and the transformer decoupling to get a sufficient performance.

4.2.3.2 Transit time spread

We also evaluated the transit time spread of the 1p.e. signal in different HV. The 20MHz low pass filter is still used in this study.

The transit time distribution (e.g. Fig. 4.18) is fitted with Exponential Modified Gaussian. The TTS at each HV is shown in Fig. 4.19. We can see that the TTS decreased

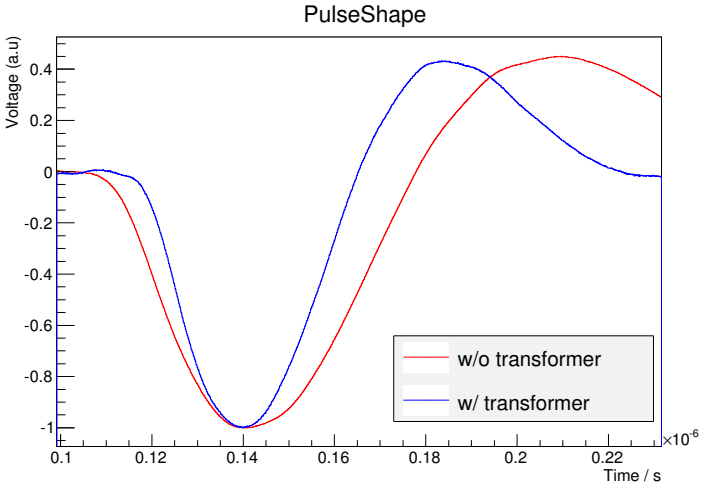

FIGURE 4.14: The effect of decoupling transformer on pulse shape of HPD signal
HPD: 50 cm HPD w/ ϕ14.7 mm AD, HV: 11 kV AD Bias V: 415 V, Bandwidth: 20 MHz

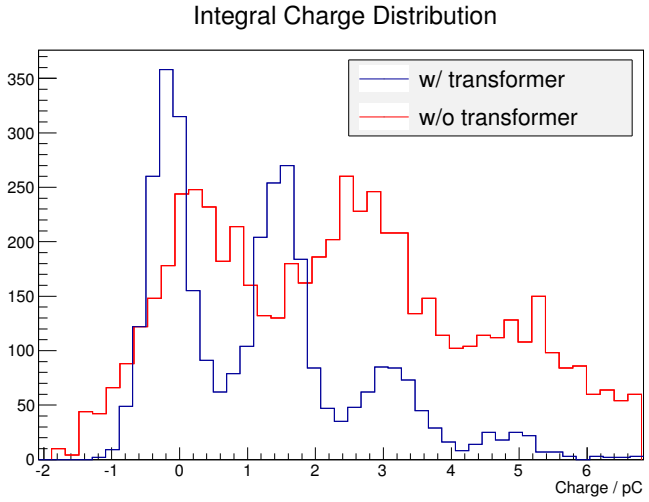

FIGURE 4.15: The effect of decoupling transformer on the integral charge distribution of HPD signal
HPD: 50 cm HPD w/ ϕ14.7 mm AD, HV: 11 kV AD Bias V: 415 V, Bandwidth: 20 MHz

with the HV increased until 10kV. As has been stated in Section 3.2.2, the intrinsic time performance of AD is excellent so the time performance of HPD is mainly constrained by the preamplifier. Besides the time response of preamplifier, the noise level of preamplifier is another important factor which can influence the TTS. It is known that the transit time is determined by the time when the signal reaches the threshold. Therefore, for a lower HV, in other words, a lower gain and a lower pulse height, the smearing on the pulse shape due to the noise is stronger. As a result, when HV is lower than 10kV, the TTS is mainly influenced by the noise level, which has lower influence for the higher

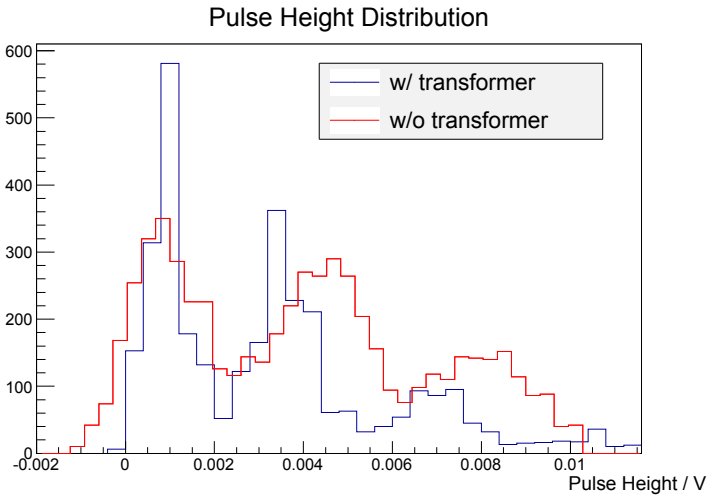

FIGURE 4.16: The effect of decoupling transformer on the pulse height distribution of HPD signal
HPD: 50 cm HPD w/ ϕ14.7 mm AD, HV: 11 kV AD Bias V: 415 V, Bandwidth: 20 MHz

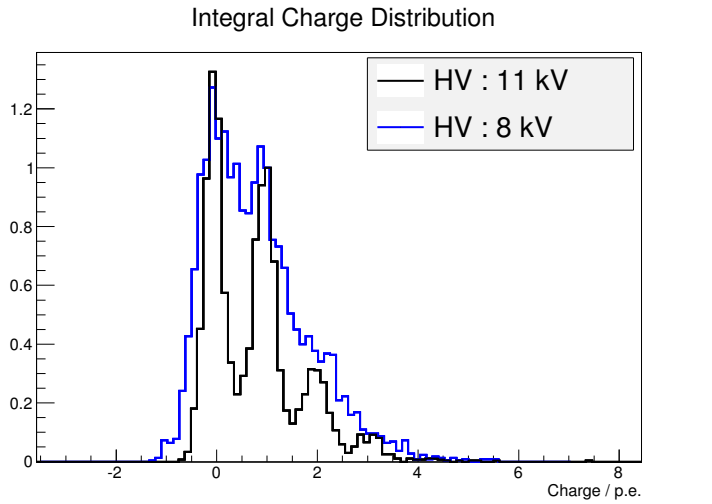

FIGURE 4.17: Integral charge distribution of the signal of the 50 cm HPD with ϕ14.7 mm AD with decoupling transformer
AD Bias V: 415 V, With Decoupling Transformer, Bandwidth: 20 MHz

HV. When the HV is higher than 10kV, the TTS is dominated by other factors, such as the variation of the real threshold on the pulse shape due to the baseline shift. Because the time response of preamplifier is slow, the change of the threshold will influence the time when the signal reach the threshold.

Based on the same reason, this value can be improved by redesigning the preamplifier, including the suppression of the noise level and making the response faster.

TABLE 4.3: Single photoelectron of 50 cm HPD w/ 14.7mm AD and decoupling transformer

	50 cm HPD w/ 14.7mm AD and trans	50 cm HPD w/ 5mm AD [2]	SK PMT	Hyper-K Requirement
Rise Time (ns)	14.3	7.4	10.6	10
Fall Time (ns)	16.7	11.5	13.1	-
Pulse width (FWHM) (ns)	29.5	17.1	18.5	-
1p.e. resolution (σ/μ)	51.7%	16%	53%	50%
Peak / Valley	1.08	4.0	2.2	1.9

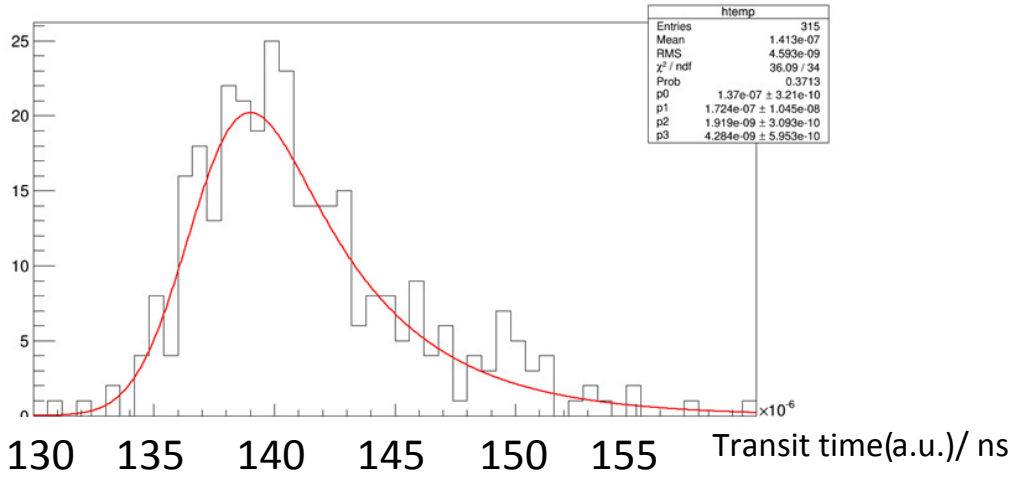

FIGURE 4.18: Transit time distribution of 50 cm HPD with 14.7 mm AD and the decoupling transformer
The red line is the fitted Exponential Modified Gaussian function.
HV: 8 kV, AD Bias V: 415 V, With Decoupling Transformer, Bandwidth: 20 MHz,

4.2.3.3 Dark count rate

For the estimation of the dark count rate, it is hard to use the discriminator to select the single p.e. signal from the noise because there are still some noise with high frequency (100 kilo-pulse per second, $\sim$ 80 MHz) (Fig 4.20), which might come from HV module. As a result, we recorded the waveform with a long gate (50μs), then applied the cut on the both of the wave height and integrated charge of the pulse to get the dark count from the electronic noise (Fig. 4.21)and counted them. The dark count rate in different HV is shown in Tab. 4.4. According the dark count rate at 8 kV, the 50 cm HPD with ϕ20 mm AD can be estimated to be 9.4 kHz according to the collection efficiency (83% for the 50 cm HPD with ϕ14.7 mm AD, 93.3% for the 50 cm HPD with ϕ20 mm AD). The

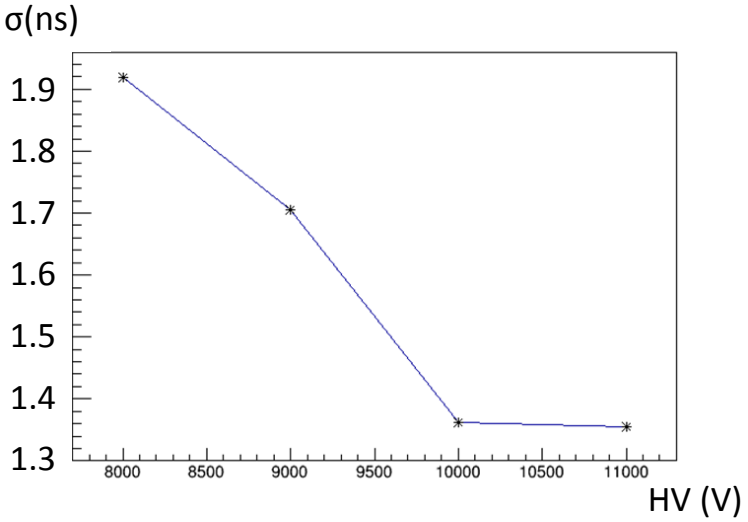

FIGURE 4.19: Transit time spread σ in different HV
HPD: 50 cm HPD w/ ϕ14.7 mm AD, AD Bias V: 415 V, With Decoupling Transformer, Bandwidth: 20 MHz,

estimation value of is consistent with the estimation result described in Section 3.2.4.

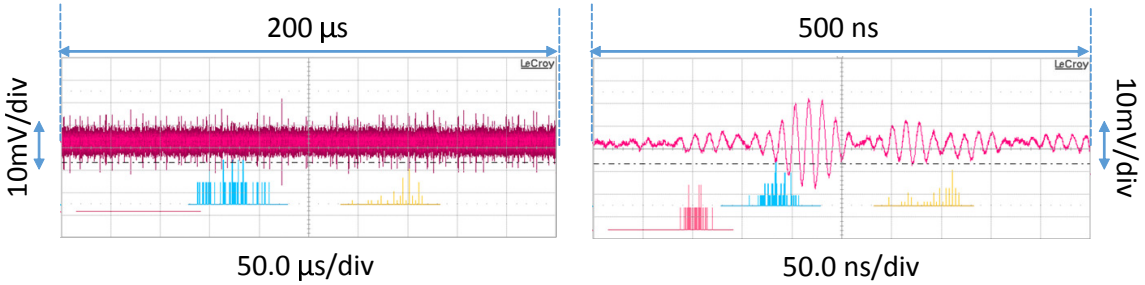

FIGURE 4.20: Remained high frequency noise
The right figure is the zoomed part of the left figure.
HPD: 50 cm HPD with ϕ14.7 mm AD, HV: 11 kV, AD Bias V: 415 V, With Decoupling Transformer, Bandwidth: Full,

TABLE 4.4: Dark count rate in different HV of 50 cm HPD with 14.7mm AD

HV	8kV	9kV	10kV	11kV
Dark Rate	8.33kHz	13.1kHz	13.8kHz	47.3kHz

AD Bias V: 415 V, With Decoupling Transformer, Bandwidth: 20 MHz

4.2.3.4 Effect of a co-axis signal cable

Furthermore, the co-axis cable can act as a low pass filter due to the condenser between the inner conductor (signal line) and the outer conductor (ground line). A 70m co-axis cable, which is similar to the cable used in Super-Kamiokande, is used as the low pass filter. The effect of the cable low pass filter is shown in Fig 4.22 and Tab. 4.5. The S/N

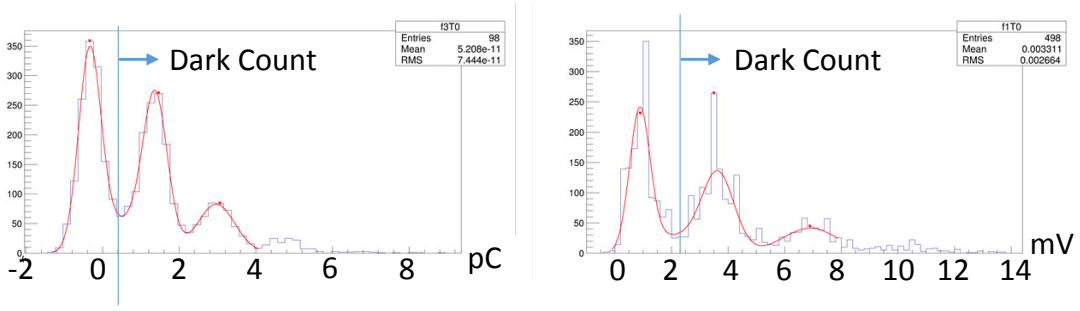

FIGURE 4.21: Cut for select dark count from electronic noise
This is an example to demonstrate how to apply cut to select dark count.
Left figure shows the integral charge distribution.
Right figure shows the pulse height distribution
HV: 11 kV, AD Bias V: 415 V, With Decoupling Transformer, Bandwidth: 20 MHz,

is increased after through 70m signal co-axis cable. However, it is still difficult to select the dark count with discriminator only. By the way, the difference of the value at the 4m row in Tab. 4.5 from previous result such as Tab.4.3 is due to the low pass filter on the oscilloscope. It should be noticed that no low pass filter on the oscilloscope is applied in the result shown in Fig. 4.22 and Tab. 4.5, while a 20MHz low pass filter is applied in the result shown before.

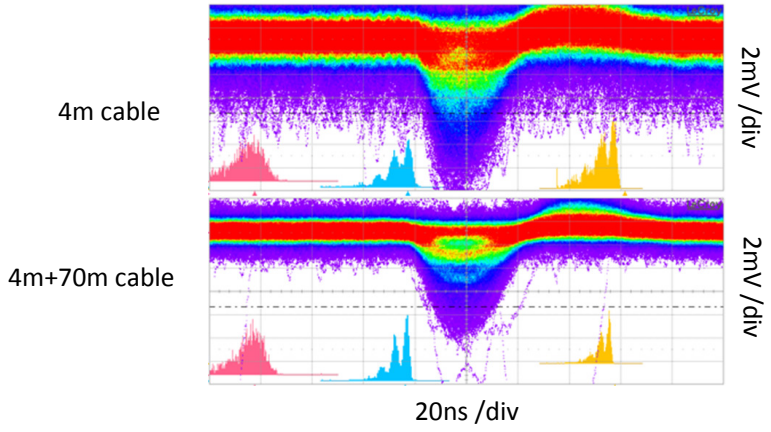

FIGURE 4.22: Effect of 70m co-axis signal cable
HPD: 50 cm HPD w/ ϕ14.7 mm AD, HV: 11 kV, AD Bias V: 415 V, With Decoupling Transformer, Bandwidth: Full,

TABLE 4.5: Effect of 70m co-axis signal cable

	Noise	1p.e. signal	1p.e. resolution	P/V	S/N
w/o 70m cable	0.28pC	1.08pC	37.1%	1.60	3.85
w/ 70m cable	0.20pC	0.89pC	31.6%	2.49	4.45

HPD: 50 cm HPD w/ ϕ14.7 mm AD, HV: 11 kV, AD Bias V: 415 V, With Decoupling Transformer, Bandwidth: Full,

4.3 Summary of R&D of 50 cm HPD with a large area AD

Based on the various experiences of the 20cm HPD and the 50 cm HPD with 5mm AD, we produced the prototype of the 50 cm HPD with 20mm AD, our target design. A higher noise level is observed because of the larger AD junction capacitance. Two solutions: the development of a new kind of preamplifier with decoupling transformer and the development of a multi-channel AD have been proposed to resolve this issue. It is demonstrated that these two solutions can decrease the noise level effectively. However, some issues such as remained high frequency noise and strong overshoot still need to be resolved. The development of 50 cm HPD with a large area AD is still ongoing. Combination use of the multi-channel AD and the transformer decoupling is expected to give a sufficient performance required by the Hyper-K experiment. By the way, all the evaluation described in this Chapter is done in room temperature $\sim 25°C$), according the result of the temperature dependence of S/N ratio (Section 3.1.3) and P/V value (Section 3.1.4) of 20cm HPD, the performance of 50 cm HPD is expected to be better when it operates in the Hyper-K environment.

Chapter 5

R&D of High Voltage Supply

5.1 Selection of high voltage module

The output and noise of high voltage module will influence the performance and the lifetime of the HPD greatly. In order to maximize the reliability, including stability, long-term durability and high performance, of HV module, several HV module products were designed and produced independently. The best one will be chosen. In this section, two HV modules from different companies were installed into 20cm HPD and evaluated.

5.1.1 Performance evaluation after installed into HPD

The basic performance, including the HV output, LV output, output timing response after enable or disable, of two HV Module (A and B), which are made by different companies were tested.

After the confirmation of their linearity and the timing response of HV output, these two HV modules were installed into a same HPD one after another to evaluate its influence on the single photon response of HPD (EHD0099).

Figure 5.1 shows the single p.e. response of HPD with each HV module. Both of them have good performance (Tab. 5.1). In the future, these HV modules will be evaluated from the aspect of lifetime and stability. A way to evaluate the lifetime of HV modules is shown in Section 5.3.

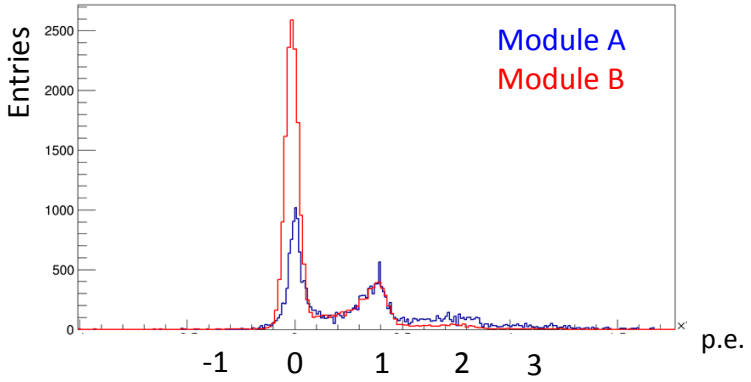

FIGURE 5.1: Single p.e. response of HPD with each HV module
The single p.e. peaks are similar. The difference of the pedestal peak is due to different luminosity.
HV: 8 kV, LV: 300 V

TABLE 5.1: Single p.e. response of HPD with each HV module

	Noise (σ_{ped})	single p.e. resolution (σ/μ)
Module A	0.21pC	12%
Module B	0.28pC	15%

HV: 8 kV, LV: 300 V

5.2 External HV supply

It is difficult to repair or exchange the HV module if it is mounted in the HPD, which is fixed in the water tank. The possibility of external HV supply is also in consideration. However, the HPD needs a higher voltage ($\sim$ 8 kV) than the PMT used in SK (2 kV). New HV cable and connector need to be developed and evaluated.

A candidate of the HV cable is developed (Fig 5.2, Tab 5.2). 40m of the cable is connected to a 20cm HPD (EHD0099) and its single p.e. response was measured. Fig. 5.3 and Tab. 5.3 shows the charge distribution and the wave height distribution. It is obvious that both of the signal and the noise didn't change a lot.

5.3 On-off resistant

As has been stated above, the photosensor will be used over 10 years in Hyper-K, which means that the lifetime and the stability of photosensor are very important. The on-off resistant evaluation by observing the performance variation with frequent on-off cycling,

FIGURE 5.2: HV cable

TABLE 5.2: Specification of the HV cable

Item	Value
Outer diameter of conductor	0.38mm
Outer diameter of insulator	1.00mm
Resistance of conductor	$< 228\Omega$ / km
Resistance of insulator	$> 1000M\Omega \bullet km$
Maximum operating voltage	12kVdc
Maximum operating current	100uAdc
Maximum bending radius	8mm

TABLE 5.3: Effect on single p.e. response of 70m HV cable

	Noise (σ_{ped})	single p.e.	single p.e. resolution (σ/μ)
Internal HV supply	0.21pC	2.6pC	12%
External HV supply (40m HV cable)	0.24pC	2.7pC	17%

HV: 8 kV, LV: 300 V

is an easy way to estimate the lifetime and the stability of HPD. As the first step, we studied the on-off resistant of one HV module. Setup of test is shown in Fig. 5.4. A USB module (NI, USB-6001) is used to control and monitor the HV module output. We alternated the enable switch of HV module every 30s.

After 80, 000 times of on-off cycle for 4 weeks, the HV module can still output normally without exception. Even the photosensor will be turned on or turned off every day, the HV module can still operate more than 200 years.

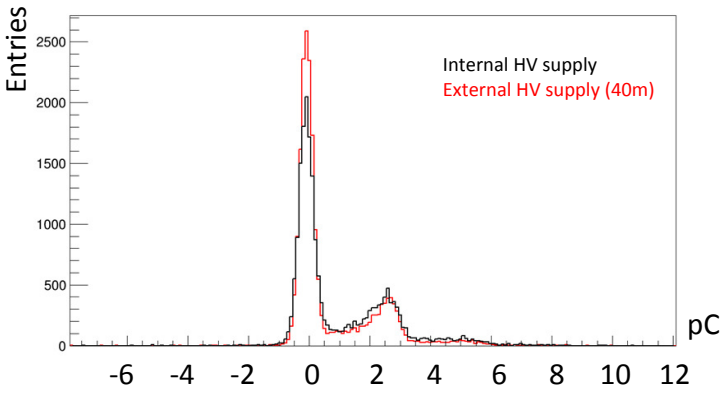

FIGURE 5.3: Effect on single p.e. response of 70m HV cable
HV: 8 kV, LV: 300 V

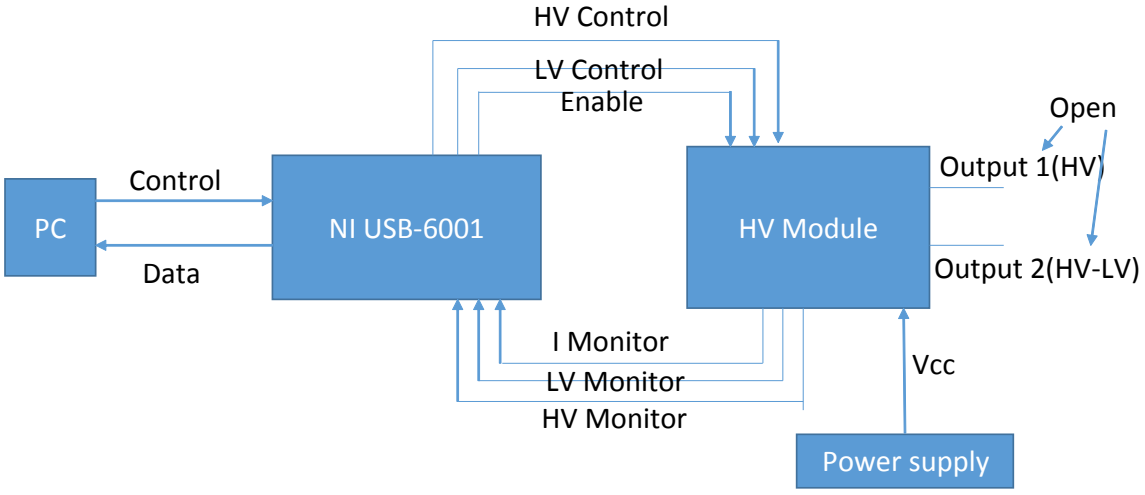

FIGURE 5.4: Setup for On-Off resistant measurement

In the future, the long-term stability, the performance of the HV module in high water pressure ($\sim$ 1 MPa)will also be tested.

5.4 Summary of R&D of High Voltage supply

The development and evaluation of HV supply is ongoing. Best one will be chosen in some candidates developed separately after considering the stability, long-term durability, noise level. The HV cable and connector for the external HV supply option are also under development. The performance of the HV cable in the water will also be tested in the future.

Chapter 6

Summary and future prospects

6.1 Summary

The Hyper-Kamiokande detector is a proposed next generation underground water Cherenkov detector. It can serve as a detector capable of observing accelerator, atmospheric and solar neutrinos, proton decays, and neutrinos from other astrophysical origins, therefore provides rich scientific programs, including the decision of mass hierarchy of neutrino, CP violation in lepton section, supernova neutrino and the validation of grand unified theory.

To further improve the sensitivity of new physics, a new photo-detector with better performance than the photomultiplier tube used in Super-Kamiokande, is desired. Three kinds of new high QE version PD: Venetian Blind PMT, Box & Line PMT and HPD, were developed and evaluated. The HPD uses the AD instead of the dynodes which are often used by PMT so that it has a simpler structure. However, it is the first time to apply a large aperture HPD in the water Cherenkov detector. As a first step, we developed the 20cm HPD with 5mmϕ AD and evaluated its performance. Based on the development experience, a larger photocathode HPD, the 50 cm HPD with 5mmϕ AD, is developed and evaluated. In order to ensure the collection efficiency of the 50 cm HPD, our target design, we produced the prototype of the 50 cm HPD with 20mmϕ AD.

For the 20cm HPD with 5mmϕ AD, the basic performance has been evaluated fully[1] and it is showed that the HPD has lower dark rate, better single p.e. energy and time

resolution than that of SK PMT (Tabl. 2.1) in the room temperature. In Section 3.1, we can see that the HPD have a better performance in the temperature of Hyper-K ($\sim$ 13 °C) than that in the room temperature. The temperature dependency of gain is stronger when the AD bias voltage is higher. A typical temperature coefficient is $-2.4\%°C$ (-2.6% °C) when the AD bias voltage is 300V (400V) for 5mmϕ AD (20mm ϕ AD). This result can be also used for calibration in the future.

For the 50 cm HPD with 5mmϕ AD, the detailed performance, including linearity, time resolution and dark count rate, is evaluated in Section 3.2. The linearity is confirmed in 3% up to 140 p.e, due to the preamplifier output constraint, which doesn't satisfy the requirement of the photosensor for Hyper-K yet. The time resolution of 50 cm HPD with 5mmϕ AD (1.15ns @ 1p.e.) is better than that of SK PMT (2.2ns @ 1 p.e.). The 50 cm HPD with 5 mmϕ AD has a dark count rate of 0.8 kHz. After considering the collection efficiency of this HPD, the dark count rate of the 50 cm HPD with 20 mmϕ AD, our targe design, is estimated to be about 9.3 kHz. which is consistent with the estimation value according the result of the 50 cm HPD with 14.7 mmϕ AD. After considering the temperature dependence, the dark count rate of 50 cm HPD with 20 mmϕ AD in Hyper-K temperature ($\sim$ 13 °C) is 4.65 kHz, the same level with that of SK PMT (4.2 kHz).

Finally, for our goal, the 50 cm HPD with 20mmϕ AD, the prototype has been produced. Due to the large capacitance from the large area of AD, the signal response is slower and the noise level is higher, the development of preamplifier is therefore difficult. Some solution, such as decoupling transformer or segmented AD, have been proposed and tested. It has been confirmed that the transformer decoupling and segmented AD can improve the S/N effectively.

Besides, the optimization of the HV supply is ongoing. Two prototypes of different HV modules have been tested on a 20 cm HPD with 5 mmϕ AD and showed no significant difference on the influence to the signal response of HPD. One of the two prototypes is not broken after 80, 000 times of on-off cycle. Even the photosensor will be turned on or turned off every day, the HV module can still operate more than 200 years. Moreover, the external HV supply is also been considered. The application of HV cable with length of 40m didn't show significant influence on the single p.e. response of 20 cm HPD with

5 mmϕ AD. The external HV supply is a competitive option but more test need to be done in the future.

6.2 Future prospects

The development of 50 cm HPD with 20mmϕ AD has many progress so far and it has great potential as a Hyper-Kamiokande photo-detector.

However, for the 50 cm HPD with 20mmϕ AD, there is still some remaining issue such as strong overshoot, high frequency noise (100 kilo-pulse per second, freq: $\sim$ 80 MHz, $V_{pp} \sim$ 40 mV), and narrow dynamic range (current: $\sim$ 140 p.e., required: 1, 000 p.e.) which needs to be resolved in the future.

Furthermore, about the HV supply, both of the HV module and the HV cable need to be tested under high pressure water. The long-term stability and durability of the HV supply will also need to be tested.

Besides, many other works, such as the reduction of the radioisotope in the glass of the HPD, the improvement of the resistance to water pressure are ongoing to ensure that HPD can be used in a water Cherenkov detector with high performance and stability.

Bibliography

[1] Y. Suda. *Nuclear Instruments and Methods in Physics Research A*, 766:185–188, 2014.

[2] Yusuke Suda. *PoS*, TIPP2014:153, 2014.

[3] Hamamatsu Photonics K.K. *Photomultiplier Tubes: Basic and Applications*, page 18, 2007.

[4] E. Gatti, P.F. Manfredi, and D.Marioli. *Nuclear Instruments and Methods*, 193: 539–547, 1982.

[5] T. Yanagida M. Fukugita. *Phys. Lett. B.*, 174:45, 1986.

[6] J.H. Christenson, J.W. Cronin, V.L. Fitch, and R. Turlay. *Phys. Rev. Lett.*, 13:138, 1964.

[7] R. Davis Jr., D.S. Harmer, and K.C. Hoffman. *Phys. Rev. Lett.*, 20:1205, 1968.

[8] Y. Fukuda et al. *Phys. Rev. Lett.*, 81:1562, 1998.

[9] E. Aliu et al. *Phys. Rev. Lett.*, 94:081802, 2005.

[10] The Daya Bay Collaboration. *Phys. Rev. Lett.*, 108:171803, 2012.

[11] RENO Collaboration. *Phys. Rev. Lett.*, 108:191802, 2012.

[12] H. Ray. *hep-ex/0701040v1.*

[13] S. Sakata Z. Maki, M. Nakagawa. *Prog. Theo. Phys.*, 28:870, 1962.

[14] B. Pontecorvo. *Sov. Phys. JETP.*, 26:984, 1968.

[15] S.P. Mikheyev and A.Y. Smirnov. *Soviet Journal of Nuclear Physics*, 42:913, 1985.

[16] L. Wolfenstein. *Phys. Rev. D*, 17:2369, 1978.

[17] The T2K Collaboration. *Progress of Theoretical and Experimental Physics*, page 043C01, 2015.

[18] T. Kikawa. *Doctoral Thesis, Kyoto University*, 2014.

[19] K. Abe et al. *arXiv:1109.3262v1.*, 2011.

[20] Y. Fukuda et al. *Nuclear Instruments and Methods in Physics Research A*, 501: 418–462, 2003.

[21] K. Abe et al. *arXiv:1309.0184*, 2013.

[22] The Super-Kamiokande Collaboration. *Phys. Rev. D*, 90:072005, 2014.

[23] K. Hirata et al. *Phys.Rev.Lett.*, 58:1490–1493, 1987.

[24] R.M. Bionta et al. *Phys.Rev.Lett.*, 58:1494, 1987.

[25] E.N. Alekseev, L.N. Alekseeva, I.V. Krivosheina, and V.I. Volchenko. *Phys.Lett.B*, 205:209–214, 1988.

[26] Nathan Smith, Kenneth H. Hinkle, and Nils Ryde. *The Astronomical Journal*, 137, 2009.

[27] A. Suzuki et al. *Nuclear Instruments and Methods in Physics Research A*, 329: 299–313, 1993.

[28] Y. Kawai. *Doctoral Thesis, The Graduate University for Advanced Studies*, 2007.

[29] M.Shiozawa. *Doctoral Thesis, University of Tokyo*, 1999.

[30] S. Kobayashi, K. Yamaoka, M. Amami, and M. Kobayashi. *Nuclear Instruments and Methods in Physics Research A*, 364:95–102, 1995.

[31] K. Abe et al. *Nuclear Instruments and Methods in Physics Research A*, 737:253–272, 2014.

[32] H. Ikeda, M. Mori, T. Tanimori, K. Kihara, and Y. Suzuki et al. *Nuclear Instruments and Methods in Physics Research A*, 320:310–316, 1992.